Plastic landmark anchoring in zebrafish compass neurons

https://doi.org/10.1038/s41586-025-09888-x

Received: 17 December 2024

Accepted: 7 November 2025

Published online: 07 January 2026

Open access

Check for updates

Ryosuke Tanaka[1]✉ & Ruben Portugues[1,2,3,4,5]✉

Vision can inform animals as they navigate their environment. Landmarks can be used to maintain heading, while optic flow can be integrated to estimate turning. Although it has been shown that head direction (HD) neurons in various species use these visual cues[1,2], the circuit mechanisms underlying this process in vertebrates remain unknown. Here we asked whether and how the recently identified HD cells in the larval zebrafish[3], one of the smallest vertebrate models, incorporate visual information. By combining two-photon microscopy with a panoramic virtual reality setup, we demonstrate that the zebrafish HD cells can reliably track the orientation of multiple visual scenes, exploiting both visual landmarks and optic flow cues. The mapping between landmark cues and heading estimates is idiosyncratic across fish and experience dependent. Furthermore, we show that landmark tracking requires the lateralized projection from the habenula to the interpeduncular nucleus[4], a structure innervated by HD neuron processes[3]. The physiological and morphological parallels suggest that a Hebbian mechanism similar to the fly ring neurons[5,6] is at work in the habenula axons. Overall, our observation that hindbrain HD cells of larval zebrafish can utilize the visual cues despite the lack of an elaborate visual telencephalon sheds new light on the evolution of navigation circuitry in vertebrates.

Neurons whose activities reflect spatial relationships between animals and their environments have been identified in the brains of diverse animal species[7], probably supporting navigation. A simple example of space-tuned cells is HD cells, which persistently fire when animals are facing a particular direction[8]. Because the head direction of an animal is typically not directly provided to the sensory system, HD cells need to integrate the history of rotational movements that animals make, a process called angular path integration. As a simple, yet biophysically plausible mechanism to implement angular path integration, a class of dynamical models called ring attractors has been proposed[9]. A ring attractor typically consists of neurons arranged on a topological ring, which excite nearby neurons while inhibiting far away neurons. Such connectivity architecture gives rise to a single, persistent bump of activity on the ring in the absence of external inputs, which can be used to represent the head direction.

More than three decades of research have identified HD cells in various mammalian brain regions[10]. Yet, it has remained inconclusive where and how the tuning to head directions first emerges. A recent study on the larval zebrafish identified a group of GABAergic (γ-aminobutyric acid-dependent) HD cells in the anterior hindbrain (aHB) rhombomere 1 (ref. 3). This GABAergic nucleus is probably homologous to the mammalian dorsal tegmental nucleus (DTN)[11], one of the basal-most brain regions with HD cells in rodents[12–14]. The dendrites and axons of these zebrafish HD cells form topographically organized columns in the dorsal interpeduncular nucleus (dIPN), such that cells tuned to the opposite head directions would inhibit each other, recapitulating a key connectivity motif of ring attractors.

In addition to motor-based angular path integration, animals can also utilize visual cues, such as landmarks and optic flow, to improve their sense of heading[1,2]. In rodents, cortical visual areas (for example, the retrosplenial cortex) are thought to provide visual information to HD neurons[15]. However, unlike mammals, the larval zebrafish lacks an elaborate visual telencephalon. This raises the possibility that there exist evolutionarily older, non-telencephalic pathways that route visual information to the HD neurons in the aHB. We therefore set out to ask whether and how the larval zebrafish HD neurons utilize visual cues.

GABAergic aHB cells track visual scene orientation

The aHB rhombomere 1 of the larval zebrafish contains a group of gad1b$^+$ HD neurons[3]. The preferred headings of these HD cells are topographically arranged, such that when the fish turns rightwards, the bump of neuronal activity moves counterclockwise, as viewed from the top (Fig. 1a). Somewhat surprisingly, the previous study did not detect any effect of visual feedback on the bump movements[3]. We reasoned that this might be due to the fact that the visual stimuli were presented below the fish. Intuitively, the upper visual field seems to contain more relevant cues for orienting oneself. To achieve a panoramic presentation of visual stimuli covering the upper visual field, we built a compact projection setup composed of a single projector and multiple mirrors[16]

---

[1] Institute for Neuroscience, Technical University of Munich, Munich, Germany. [2] Munich Cluster for Systems Neurology (SyNergy), Munich, Germany. [3] Max Plank Fellow Group — Mechanisms of Cognition, Max Planck Institute of Psychiatry, Munich, Germany. [4] Bernstein Center for Computational Neuroscience Munich, Planegg-Martinsried, Germany. [5] Department of Neurobiology and Behavior, Cornell University, Ithaca, NY, USA. ✉e-mail: ryosuke.tanaka@tum.de; ruben.portugues@cornell.edu

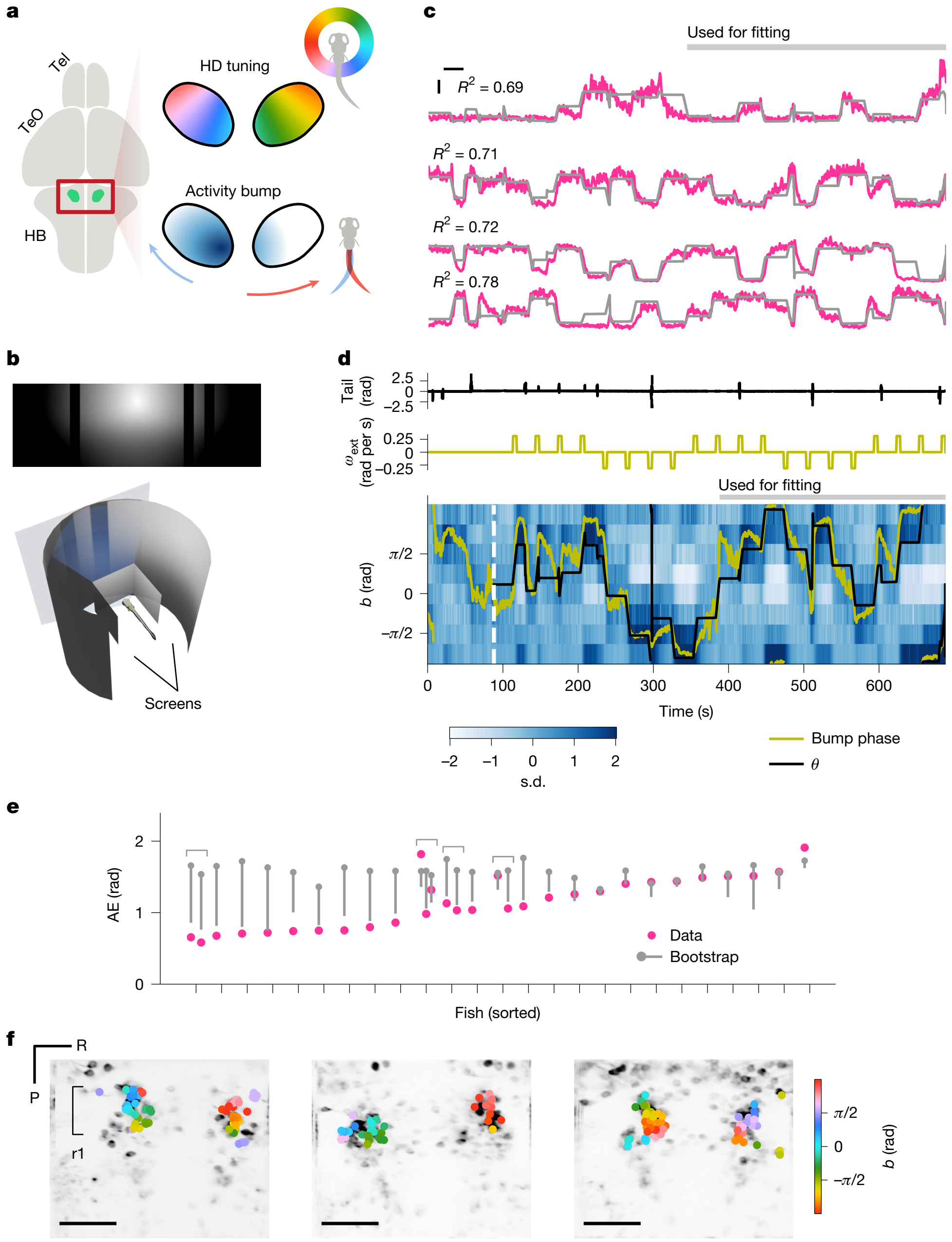

Fig. 1 | aHB GABAergic cells that track a visual scene. a, HD neurons in the larval zebrafish aHB are topographically organized by their tunings. As a result, the population activity of these cells appears as a single 'bump' that moves as the fish turns. Tel, telencephalon; TeO, optic tectum. **b**, The sun-and-bars visual scene consisting of a radial luminance gradient and dark bars (top) wrapped around the fish, forming a virtual cylinder (bottom). **c**, Example activity of the cells tuned to different scene orientations (pink) with the sinusoidal fit (grey). Only the second half of the data were used for the fitting procedure. The horizontal and vertical bars indicate 20 s and 1 s.d., respectively. **d**, Binned activity of the scene-orientation tuned cells, with the scene orientation θ (black) and the bump phase (yellow) overlaid, as well as associated traces of the tail angle (top) and the exogenous rotation velocity ω_{ext} (middle). **e**, Time-averaged absolute error (AE; that is, |bump phase − θ|) for each fish (pink) compared with the shuffle. The grey dots and bars indicate the median and 5th percentile of the shuffle distributions, respectively. Out of 25 fish, 15 showed significantly below chance AE. Note that recordings from multiple planes were made in four fish, as indicated by the brackets. **f**, Selected ROIs visualized on the anatomy, with their scene orientation tuning colour coded. Scale bars, 50 µm. P, posterior; R, right; r1, rhombomere 1.

(Supplementary Video 1). Larvae embedded in agarose observed view-corrected virtual 3D scenes projected onto the planar screens on the three sides, which covered 270° of azimuth and 90° of elevation (Fig. 1b and Methods). The neural activity was optically monitored from above with a two-photon microscope.

In this setup, we imaged the neural activity of aHB neurons expressing GCaMP6s[17] under the control of *gad1b–Gal4* (ref. 18) in 6–9 days post-fertilization larvae. Each experiment started with an alternating presentation of 8-s-long, bright and dark full-screen flashes. Naively visual neurons that reliably responded to these flashes were removed from further analysis (Methods). In the first experiment, we presented a scene consisting of a circular luminance gradient centred above the horizon and dark vertical bars (henceforth 'sun-and-bars') for 10 min (Fig. 1b). The scene wrapped around the fish, forming a virtual cylinder. The orientation of the scene was controlled in a closed-loop manner based on the tail movements. In addition, slow exogenous rotation of the scene was superimposed intermittently (90° rotations over 5 s every 30 s, switching directions every four times), such that the fish would experience various scene orientations even if they did not make many spontaneous turns. In this stimulus configuration, the behaviour of the fish was dominated by low-gain turns counteracting exogenous rotations, and they did not obviously fixate on any part of the scene (Extended Data Fig. 1). We hypothesized that in this configuration, HD cells would indeed exploit visual information, so we would expect their activity to be well fit by a single-peaked periodic function of the scene orientation. Thus, we fit a scaled, shifted sinusoid $a \times \cos(\theta - b) + c$ to one-half of the normalized fluorescence time trace of each cell. Here θ denotes the orientation of the scene relative to the fish (clockwise positive), and a, b and c represent the response amplitude, preferred orientation and baseline, respectively. We selected cells where the sinusoidal fit resulted in $R^2 > 0.15$ for further analyses. In this notation, the heading of the fish in the virtual world would be $-\theta$.

We found cells surpassing the above criteria in all fish we recorded from. In some cells, R^2 was as high as 0.8 (Fig. 1c and Extended Data Fig. 2a–c). At the population level, a single bump of activity was clearly visible, even before the onset of the sun-and-bars scene (that is, during flash presentations) (Fig. 1d, Extended Data Fig. 2d and Supplementary Video 2). We calculated the ‘bump phase’ as the angle of the activity-weighted average of the preferred orientation vectors of the selected cells[2] (Methods). We then examined the alignment between the bump phase and the scene orientation by running bootstrap tests on the portion of the data not used for the fitting. The tests revealed significant bump–scene alignment in 15 out of 25 fish (Fig. 1e), a proportion not expected from chance (Extended Data Fig. 2e). We did not find an obvious predictor of individual variability in the alignment (Extended Data Fig. 1h–j). The preferred scene orientations of individual cells exhibited a clockwise topographical organization in rhombomere 1 (Fig. 1f and Extended Data Fig. 2f), consistent with the previous observed topography of HD cells[3]. The anatomical arrangement of preferred orientations had idiosyncratic offsets across multiple fish: for example, cells with $b = 0$ can be on the left or right side of the brain. This observation indicated the possibility that anchoring of the HD cells to visual landmarks is not hard-wired, a point we return to later.

The scene tuned cells integrate turns

Although we suspect that these scene-orientation-tuned cells are HD cells, the sinusoidal-fitting procedure could also pick up visual neurons tuned to local features. To ascertain their identity as HD cells, we wanted to make sure that their bump phase moved as fish turned, even without visual feedback. In the first experiment above, we continued recordings for another 10 min in the darkness after turning off the visual scene (Extended Data Fig. 3a). However, the small number of swim bouts that fish made in the darkness made such analysis difficult. To encourage fish to turn frequently without giving them visual cues for rotation, we decided to exploit the optomotor response[19] (Extended Data Fig. 3b). The first half of the new experiment was mostly identical to that presented in Fig. 1, with a closed-loop panoramic scene with exogenous rotations. We performed the sinusoidal fitting on this half of the data to identify scene-orientation-tuned cells. During the second half, we intermittently presented an array of white dots translating sideways on a black background (in the virtual 3D space), which encouraged the fish to make turns. Once fish made a swim bout, the dots immediately disappeared without providing any rotational feedback. Here we found that the bump moved clockwise and counterclockwise as fish turned left and right, consistent with the previous observation[3] (Extended Data Fig. 3c–e). The negative correlation between the turn amplitude and bump-phase shift was statistically significant across the population (Extended Data Fig. 3f). Overall, these results suggest that the scene-orientation-tuned cells detected with the sinusoidal fits are genuine HD cells.

The same set of HD cells can track multiple scenes

In the next experiment, we asked whether the same set of HD cells can consistently represent heading direction in different visual scenes. Here the same sun-and-bar scene was presented in a closed loop with exogenous rotations. After 8 min, the scene was switched to what we named the ‘Stonehenge’ scene, consisting of multiple irregularly spaced bright vertical bars over a dark background (Extended Data Fig. 4a), while maintaining the same exogenous rotation sequence. As before, HD cells were identified with the sinusoidal fits on the sun-and-bars half of the data (Extended Data Fig. 4b,f). To test whether the bump phase still tracked the new scene, we fit von Mises distributions on the histogram of the offset between the scene orientation and bump phase (Extended Data Fig. 4c) and performed bootstrap tests with time-domain shuffling on the κ parameter, which controls the peakiness of the distribution. Here, 8 out of 20 fish exhibited significantly above chance κ (Extended Data Fig. 4d), a higher proportion than expected by chance (Extended Data Fig. 4g). The mean offset between the scene orientation and the bump offset varied across fish, albeit with a bias probably due to the cross-correlation between the scenes (Extended Data Fig. 4e).

In a separate experiment, we also tested whether fish are capable of tracking scenes with visual landmarks only in the upper or lower visual fields. We found that, even though some individual fish can utilize either upper or lower landmarks, more fish were able to track the upper landmark (Extended Data Fig. 4h–m), confirming the initial intuition behind our decision to build the panoramic setup. Together, these results demonstrate the capacity of the HD cells to maintain stable head direction representations in various visual scenes.

HD cells exploit visual landmarks and optic flow

How these HD neurons track multiple visual scenes remains unknown. An early ring attractor model[9] proposed two separate mechanisms: first, the model assumes an array of visual neurons that tile the visual space and detect landmarks, which instruct the activity bump to be at a specific phase (Fig. 2a). Second, the model assumes two additional rings of neurons (‘rotation cells’), which connect neighbouring HD neurons in a clockwise-shifted or counterclockwise-shifted manner, respectively. The activities of these rotation cells are further assumed to be gated by inputs from cells encoding the angular head velocity of animals. As a result, when the animal turns (for example, rightwards), the clockwise rotation cell at the current bump phase is activated, causing the bump to drift counterclockwise (Fig. 2b). Although the original model primarily considered the vestibular system to be the source of the angular head velocity information, rotational optic flow can also inform the animal of their angular head velocity. To test whether the zebrafish HD neurons use either the visual landmark-based or optic flow-based mechanisms (or both), we designed a new experiment with three epochs (Fig. 2c). In the first (‘smooth’) epoch, the sun-and-bars scene was presented in a closed-loop with superimposed slow exogenous rotations as before. HD cells were identified by performing the sinusoidal fitting on this portion of data. In the second (‘jump’) epoch, exogenous rotations were substituted by abrupt jumps of 90° without any intervening smooth rotation, eliminating the optic flow cues. In the final (‘noise’) epoch, the visual scene was swapped with a featureless spatial noise pattern, but with a smooth rotation sequence. If the HD cells exclusively relied on either optic flow-based or landmark-based mechanisms, we would expect them to lose track of the scene orientation in the jump or noise epochs, respectively.

Figure 2d shows an example fish whose HD cells appeared to track the scene orientation well in both jump and noise epochs (see also Extended Data Fig. 5a). In 14 out of 24 fish, the bump phase remained significantly aligned to the scene orientation in the jump epoch, a higher fraction than expected by chance (Fig. 2e,f and Extended Data Fig. 5c).

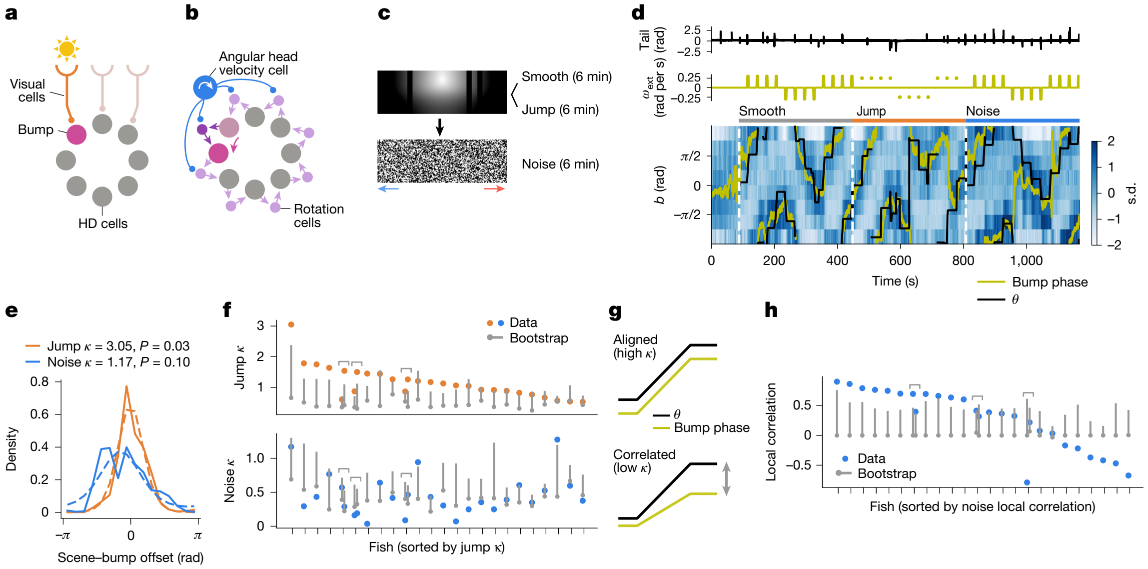

Fig. 2 | The HD neurons can exploit both landmark and optic flow cues. **a**, Visual neurons detecting landmark cues can instruct the bump phase. **b**, Rotational optic flow can move the bump by activating the rotation cells through angular head velocity cells. **c**, Schematic of the experiment. The sun-and-bars scene was presented with smooth motion (6 min) and with jumps (6 min) and was followed by a noise stimulus that rotated consistently leftwards or rightwards around the fish, as indicated by the blue or red arrows, respectively (6 min). **d**, An example single fish data, showing the tail angle (top), exogenous rotation velocity ω_{ext} (middle) and the binned HD cell activity with the scene orientation θ (black) and the bump phase (yellow; bottom). Abrupt jumps of the scene are indicated by the dots in the middle plot. The white dotted lines indicate the beginning of each experimental epoch (that is, smooth, jump or noise). **e**, The histograms of the scene–bump offset during the jump (orange solid line) and noise (blue solid line) epochs, with von Mises distributions fit to them (dotted lines). The P values are from bootstrap tests (Methods) and represent the probability that the κ exceeded the shuffle. **f**, κ from the von Mises distributions fit on the scene–bump offset histogram for each fish for each condition (orange dots for jump and blue dots for noise). The shuffle distributions are indicated in grey (dot for the median and the bar for the 95th percentile). For the jump epoch, 14 out of 24 fish showed significantly above change κ, whereas only 3 fish did so for the noise epoch. Note that multiple recordings were made in three fish, as indicated by brackets. **g**, If rotational optic flow moves the bump in the right direction but by an incorrect amount, the bump phase and the noise scene orientation will no longer be aligned but remain positively correlated. **h**, Local correlation (that is, median Pearson correlation between θ and the bump phase within 15-s-windows around the exogenous rotation episodes) in the noise epoch (blue) compared with the bootstrap distribution (grey dot denotes the median and the grey bar indicates the 95th percentile). Of 24 fish, 12 showed significantly above chance positive correlation.

By contrast, only three fish managed to maintain a constant offset between the bump phase and the scene orientation in the noise epoch (Fig. 2d). Yet, it is still possible that the rotational optic flow moved the bump in the correct direction, but not necessarily for the correct amount, making the bump-scene offsets variable (Fig. 2g). Indeed, in 12 out of 24 fish, the bump phase and the scene orientation were significantly positively correlated within short (15 s) periods of time around the exogenous rotation episodes in the noise epoch (Fig. 2h), a fraction not expected from chance (Extended Data Fig. 5b,c). The gain from the rotational optic flow to the bump-phase movement was on average about 50% (Extended Data Fig. 5d–g). Overall, these results indicate that mechanisms to exploit both visual landmarks and optic flow cues exist in the circuit surrounding the larval zebrafish HD neurons.

Scene symmetry disrupts landmark anchoring

Ring attractor models[5,6,9] hypothesize that a unique mapping from visual landmarks to the HD cell activity bump is learned (Fig. 3a). The starting point is an array of visual neurons with local receptive fields that have weak, uniform connectivity to the entire array of the HD neurons. As the animal explores the environment, the activity of each HD neuron will consistently coincide with the response of a specific visual neuron to distant, stable landmarks (such as the Sun). For example, if the Sun is setting on the western horizon, the west-tuned HD neuron would be co-active with the visual neurons with frontal receptive field, and the north-tuned HD neurons with the left-looking visual neurons, and so on. Through Hebbian plasticity at the visual-to-HD synapses, a unique mapping from the landmark bearing to the bump phase would be established. We made sure that a ring attractor with such Hebbian plasticity can indeed replicate the results in Figs. 1 and 2 and Extended Data Fig. 4a–g (Extended Data Fig. 6a–j and Supplementary Note 1).

To test whether the mapping of visual landmarks onto the larval zebrafish HD system is plastic, we challenged the HD cells with a symmetric scene, as has been done in *Drosophila*[5,6] (Fig. 3b). The experiment consisted of three epochs: in the first (pre-learning) and last (post-learning) epochs, fish observed the scene consisting of a single radial gradient of luminance in the upper visual field, mimicking the Sun. During the second (learning) epoch, a second sun was added to the scene azimuthally 180° away from the first one, introducing a twofold point symmetry in the scene. Here the two suns would simultaneously drive the bump to be at two diametrically opposite phases, between which the bump could alternate, for example (Fig. 3a). In addition, because each HD neuron would be now always co-active with two visual neurons, the Hebbian rule predicts the visual-to-HD connectivity to become doubled (Fig. 3a and Extended Data Fig. 6k,l). Once such doubled connectivity is established, a single sun would now drive the bump to the two opposite phases, degrading the scene–bump alignment (Fig. 3a and Extended Data Fig. 6m,n).

Here we identified HD cells with the sinusoidal fitting using one-half of the pre-training epoch data. Figure 3c shows the data from an example fish. During the pre-learning epoch, the bump phase and the scene orientation aligned well, and the scene–bump offset showed a clear single peaked distribution centred at 0 (Fig. 3d). During the learning epoch, the scene–bump offset became variable (Fig. 3c,d), even though the correlation structure among the HD cells was maintained (Extended Data Fig. 7a). In the post-learning epoch, the scene–bump offset distribution widened (Fig. 3d). Across all fish, the scene–bump offset spent significantly more time in the out-phase range (that is, absolute

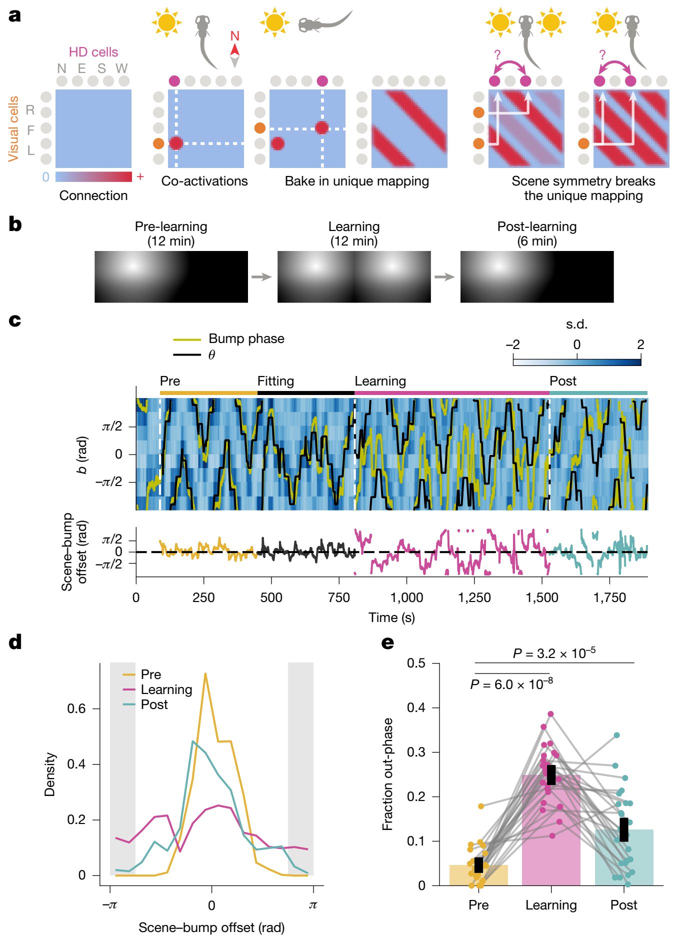

Fig. 3 | Symmetric scenes disrupt the landmark anchoring to the HD neurons. **a**, Schematics showing how the unique mapping between visual landmarks and the bump phase could be learned and disrupted by a symmetric scene. E, East; F, front; L, left; N, North; R, right; S, South; W, West. **b**, Schematic of the experiment. **c**, Data from an example fish. The binned activity of the HD cells, with the scene orientation θ (black) and the bump phase (yellow) overlaid (top). The HD cells were detected using the second half of the pre-learning epoch. The offset between the scene orientation and the bump phase over time (bottom). The white dotted lines indicate the beginning of each experimental epoch (that is, pre-learning, learning or post-learning). **d**, The histograms of the scene–bump offset for each epoch, from the fish shown in panel **c**. The grey shaded areas indicate the out-of-phase range (|scene–bump offset| > $3\pi/4$). **e**, The fraction of time that the scene–bump offset spent in the out-phase range for each epoch. The dots indicate individual fish, and the grey lines connect the same fish. *P* values are from the signed-rank tests. $n = 25$ fish.

scene–bump offset > $3\pi/4$) (Fig. 3e). A similar increase was not observed in the control group that experienced only the single sun scene throughout (Extended Data Fig. 7b–e). Overall, these results support the idea that the connectivity from the visual to HD neurons is experience dependent.

Twofold remapping in symmetric scenes

Although the experiment above clearly demonstrated the plasticity in the landmark-to-bump mapping, we were puzzled as to why the scene–bump offset never appeared bimodal in the symmetric scene (Extended Data Fig. 7f), as predicted from the 'flip-flop' scenario (Fig. 3a). To gain better insight as to how the HD cells behaved in the symmetric scene, we plotted the tuning curve of individual HD cells in each epoch (Fig. 4a and Extended Data Fig. 7g). Here, as expected, the tuning of the HD cells during the learning epoch appeared bimodal, which was significantly better fit by sinusoids of 2θ rather than of θ (Fig. 4b). However, unexpectedly, the tuning of the HD cells in the symmetric scene appeared not simply doubled, but also rotated in a systematic way according to their preferred scene orientation (Fig. 4a). In particular, pairs of HD cells with the opposite tuning appeared to rotate their tuning for a total of 90°, such that they can remain anticorrelated in the symmetric scene (Fig. 4c). Indeed, the amount of the relative tuning rotation between pairs of HD cells in the symmetric scene was proportional to their tuning difference in the single-sun scene, with a slope of −0.5 (Fig. 4d,e). This slope, which would be expected to be 0 if there was no tuning rotation, was significantly below 0 (Fig. 4f).

The population-level consequence of this ordered tuning rotation is that, in the symmetric scene, 180° of the visual scene is mapped on to the full 360° array of the HD neurons. This can be most intuitively seen by plotting the scene orientation θ and the bump phase as a scatter plot: in the symmetric scene (that is, the learning epoch), the bump phase hugs the line with slope 2 (bump phase $\equiv 2\theta \pmod{2\pi}$) instead of the diagonal (bump phase $\equiv \theta \pmod{2\pi}$; Fig. 4g), which explains why the bump–scene offset (which corresponds to the spread of dots along the diagonal) never appeared bimodal (Extended Data Fig. 7f). Instead, the offset between the bump phase and 2θ was single peaked (Fig. 4h) and significantly well fit by a von Mises distribution in 17 out of 25 fish (Fig. 4i), a higher proportion than expected by chance (Extended Data Fig. 7h). Overall, this stretched remapping phenomenon demonstrates the remarkable ability of the HD cells to capture the correlation structure in the visual neuron activities in a plastic way.

Landmark anchoring requires the visual habenula

Finally, we asked how visual information reaches the HD neurons. We hypothesized that the habenula provides HD neurons with information about visual landmarks. The habenula is a conserved epithalamic nucleus that sends dense bundles of glutamatergic axons to the IPN[20] (Fig. 5a). In particular, the dIPN, where the HD cell processes reside, receives asymmetric projections from the left dorsal habenula[4], which is enriched with light-responsive cells[21,22] that have local visual receptive fields[23]. In addition, the axon terminals of individual habenula cells wrap around the entire lateral extent of the dIPN neuropil[24], contacting the whole suite of the HD cell dendrites[25]. This all-to-all connectivity between the visual and HD neurons is well suited to implement the Hebbian landmark anchoring in the ring attractor model[9] (Fig. 3a).

To make sure that the habenula neurons have enough visual information to encode the scene orientation, we first measured visual responses of habenula neurons expressing GCaMP6s under the control of vglut2a–Gal4[26] ($n = 6$) or another enhancer-trap line (18107–Gal4; $n = 2$). By presenting vertical or horizontal bright bars against a dark background at various azimuths and elevations, we found that the left habenula is enriched with cells with local, sustained, ON receptive fields (Extended Data Fig. 8a–c), in line with previous studies[21–23]. Next, we presented the sun-and-bars scene rotating slowly (9° s^{-1}) about the fish in an open loop for four cycles in alternating directions, while recording the habenula activity (Extended Data Fig. 8d). We found that the scene orientation can be accurately decoded from the ongoing habenula activity with a naive pattern-matching algorithm (Extended Data Fig. 8e,f), suggesting that the habenula cells indeed collectively encode enough visual information to disambiguate the scene orientation, as hypothesized.

We then performed unilateral laser ablations of the habenula axons entering the IPN (see Methods for details; Extended Data Fig. 9a–f). Before and after the ablation, we repeated an experiment similar to that in Fig. 2, where the sun-and-bars scene was presented in a closed loop, with smooth rotations or abrupt jumps superimposed intermittently (Fig. 5b). In the example fish shown in Fig. 5c,d, the ablation of the visual habenula axons abolished the alignment between the scene orientation and the bump phase in both epochs, even though the bump of activity itself is still clearly visible[23]. This decrease was not observed

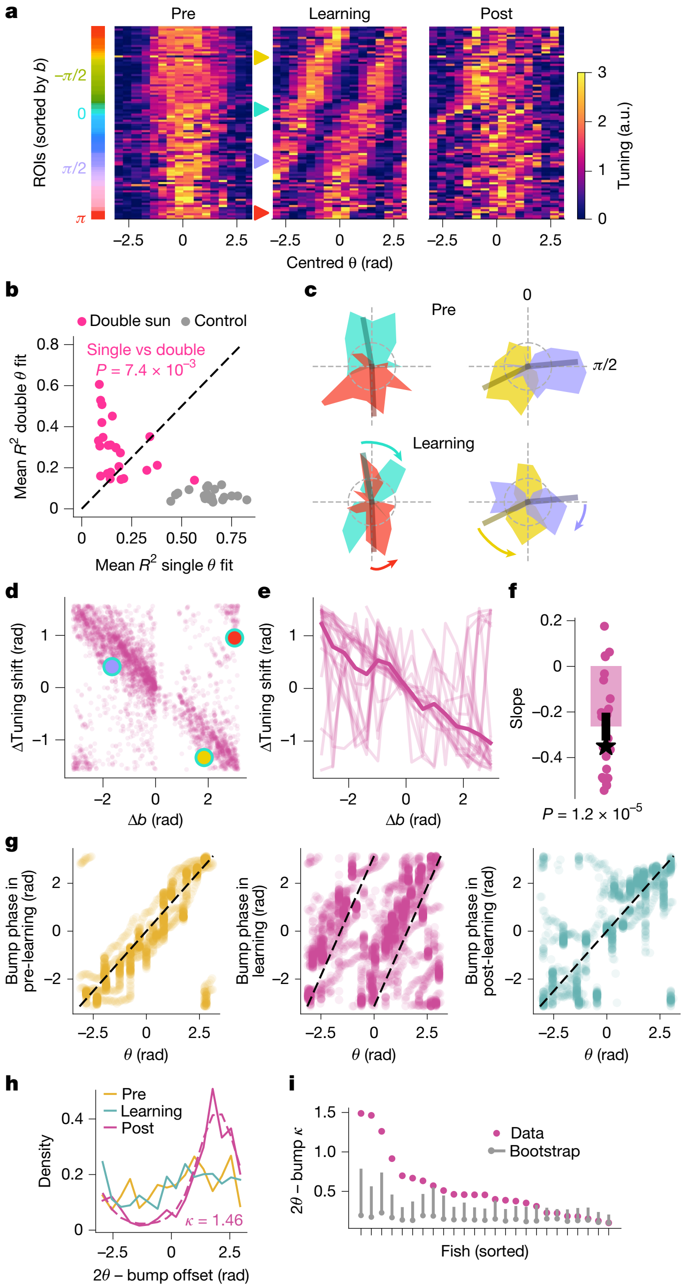

Fig. 4 | Stretched remapping in the symmetric scene. a, The tuning of the individual HD neurons in each epoch, from the same fish as in Fig. 3b. The tuning is centred to and sorted by the preferred orientation b. **b**, R^2 from sinusoidal fits by θ or 2θ on the individual HD cell tuning curves during the learning epoch, averaged across cells within fish. The pink and grey dots represent fish from ‘double-sun’ and control groups, respectively. The fit with 2θ resulted in higher R^2 for the double-sun group, from a signed-rank test (n = 25 fish). The black dashed line indicates the line along which both fits are equal. **c**, The tunings of four example cells as polar plots (indicated by triangles of matching colours in panel **a**). The dark lines indicate the mean tuning direction in the pre-learning epoch. **d**, For all pairs of the HD cells in panel **a**, the difference in the tuning rotation during the learning epoch (Δtuning shift) is plotted against the tuning difference (Δb). The red, yellow and violet dots indicate cells with matching colours in panels **a**,**c**, compared with the cyan cell. **e**, As in **d**, but for all fish, as the binned mean along the x axis (thin lines) and the average across fish (thick line). **f**, The slope between Δb and Δtuning shift for each fish (dots), as well as the population average (bar). The black star indicates the slope of the population mean (that is, the thick line in **e**). The P value is from a signed-rank test (n = 25 fish). **g**, The bump phase plotted against the scene orientation θ for each epoch, from the same fish as in panel **a**. In the pre- and post-training epochs, the black dashed lines indicate bump phase = θ, whereas in the learning epoch they indicate bump phase = 2θ (mod 2π). **h**, The histogram of the 2θ − bump offset for each epoch, as well as von Mises fit for the leaning epoch (magenta dotted line). **i**, von Mises κ fit on the 2θ − bump offset histogram (magenta dots), as well as the bootstrap median (grey dots) and 95th percentile (grey bars).

in the control-side ablated fish shown in Extended Data Fig. 9g. At the population level, the fish in the visual-side ablation group exhibited lower bump–scene alignments in both epochs, only after the ablation procedure (Fig. 5e and Extended Data Fig. 9i,j). The decrease in the bump–scene alignment was also significantly greater in the visual-side ablated group (Fig. 5f). These observations support the hypothesis that the HD neurons receive information about visual landmarks from left habenula neurons.

The aHB contains putative angular head velocity cells

In contrast to the loss of bump–scene alignment, the habenula ablation spared the visual angular path integration (Extended Data Fig. 10a–d). Thus, we wanted to explore how the rotational optic flow reaches the HD neurons. The ring attractor model (Fig. 2b) predicts the existence of ‘rotation cells’ connecting neighbouring HD neurons in an asymmetric manner, as well as angular head velocity (AHV) cells gating the rotation cells. In the last experiment, we aimed to narrow down the anatomical location of putative AHV cells. Here we reasoned that such AHV cells should be multimodal, such that they are activated when fish make turns in one direction, as well as by the rotational optic flow indicating the same body turn (Extended Data Fig. 10e). To search for putative AHV cells, we imaged various hindbrain regions in fish expressing a calcium sensor broadly (HuC–H2B–jGCaMP7c), while we presented clockwise and counterclockwise rotational optic flows, as well as translational optic flows, which were intended to encourage fish to make turns. We selected cells that reliably responded to the rotational stimuli in a direction-selective manner and examined their bout-triggered activities during the translational flow presentation.

Across 49 recordings from 21 fish, we generally observed that hindbrain neurons prefer ipsiversive rotational optic flow as well as turns (Extended Data Fig. 10f–h and Supplementary Video 3), as previously reported[27–30]. The major exception to this pattern was the bilateral clusters of cells in the rhombomere 2/3 situated dorsoposterior to the HD cells, which preferred contraversive visual rotation, but still preferred ipsiversive turns. This pattern was consistently observed across 16 fish where we imaged this region (Extended Data Fig. 10i,j). In addition, we observed smaller clusters of cells in lateral rhombomere 1 that prefer ipsiversive optic flow and contraversive turns (Extended Data Fig. 10f–h). These cells in the vicinity of the HD neurons with reversed visuomotor contingency are strong candidates for the putative AHV cells, which would enable the multimodal angular path integration in the HD neurons through hypothetical rotation cells.

Discussion

We have demonstrated that the larval zebrafish HD neurons can incorporate both allothetic (that is, landmark) and idiothetic (that is, optic flow) visual cues into their heading estimate. In particular, we found that the plastic mapping between the scene orientation and the bump phase requires input from the visually responsive side of the habenula to the dIPN. The bulk of the physiological data was consistent with the mechanism of landmark anchoring proposed in an early modelling work[9], in which a Hebbian plasticity operating on all-to-all, visual-to-HD cell synapses bakes in a unique mapping from visual landmarks to the HD representation (Fig. 3a and Extended Data Fig. 6). The all-to-all connectivity between the habenula axons and the HD neurons in the dIPN (Fig. 5a) appears to be particularly well suited to implement this mechanism.

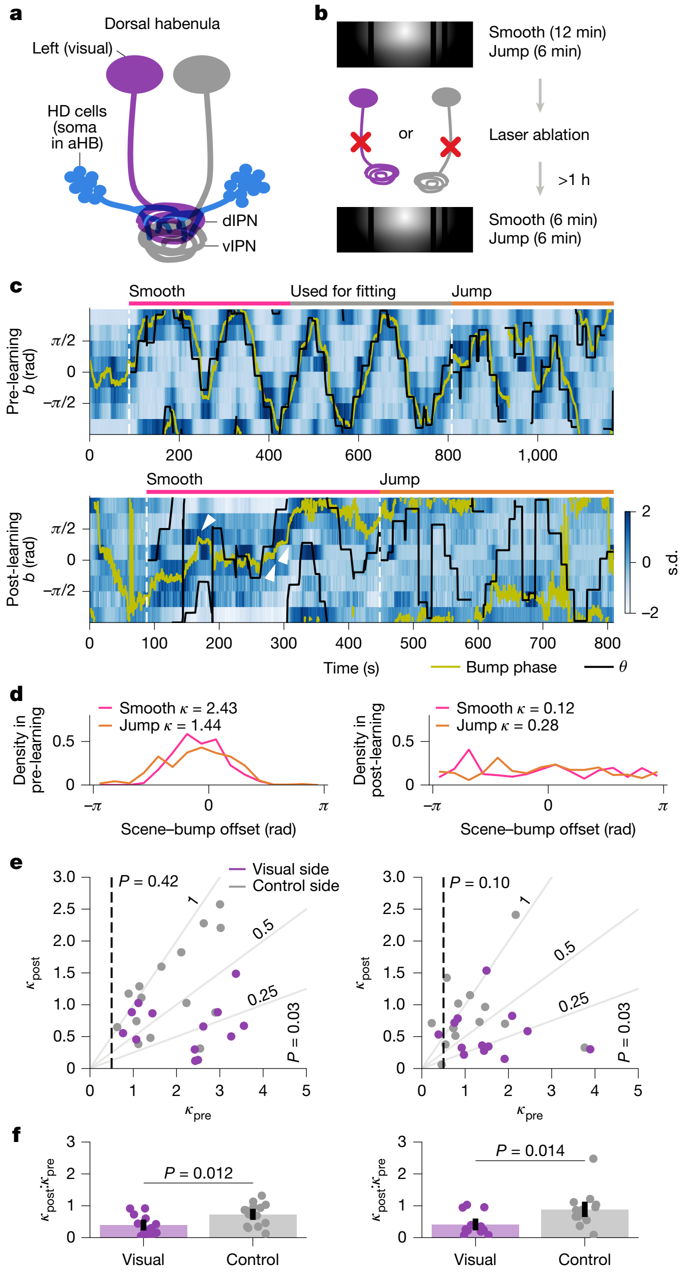

Fig. 5 | Visual habenula ablation abolishes landmark anchoring. a, Schematic of the habenulo-interpeduncular projection. **b**, Schematic of the experiment. **c**, The binned activity of the HD neurons before and after ablating the axons of the visual habenula, from an example fish. The white arrowheads indicate places where the bump phase still seemed to follow the scene rotation in the post-ablation recording. The white dotted lines indicate the beginning of each experimental epoch (that is smooth or jump). **d**, The histograms of the scene–bump offset for pre-ablation (left) and post-ablation (right) recordings, separately for smooth (pink) and jump (orange) epochs. **e**, κ of the von Mises distributions fit on the scene–bump offset histogram from the pre-ablation and post-ablation recordings, plotted against each other. The data from smooth (left) and jump (right) epochs are visualized separately. Each dot represents an individual fish, and the purple and grey dots indicate visual-side and control-side ablated animals, respectively. The thin grey lines indicate different ratios between the pre-ablation and post-ablation κ. The vertical dashed lines indicate pre-ablation $\kappa = 0.5$, and fish that did not reach this threshold were excluded when comparing pre-ablation and post-ablation κ. The P values are from rank-sum tests performed between the two ablation groups on each axis separately. $n = 13$ and 15 fish (visual side and control side, respectively) for the smooth epoch, and $n = 12$ and 13 (visual side and control side, respectively) for the jump epoch. **f**, The ratio of von Mises κ between pre-ablation and post-ablation recordings for each epoch type and ablation group. Data are mean ± s.e.m. P values are from rank-sum tests. $n = 13$ and 15 fish (visual side and control side, respectively) for the smooth epoch, and $n = 12$ and 13 (visual side and control side, respectively) for the jump epoch.

We found that, in contrast to the motion-based stabilization behaviours that rely on the lower visual field[31], upper visual field cues are more readily recognized as distal landmarks by the fish HD neurons (Extended Data Fig. 4h–m). This topographical bias probably reflects the visual ecology: reliable celestial landmarks are usually above the animals, and the limited underwater visibility would make it especially hard for aquatic animals to find reliable distal cues in the lower visual field. At the neural level, a skyward bias in the retinal ganglion cells providing visual information to the left habenula has been reported[22], consistent with our observations.

The circuit that we studied is remarkably similar to the compass system of *Drosophila*, probably due to evolutionary convergence: in *Drosophila*, HD neurons (for example, E-PG cells) project their neurites to a donut-shaped neuropil called the ellipsoid body in a topographically organized manner[2], just like the fish HD cells projecting to the dIPN. The ellipsoid body also receives axons of ellipsoid body ring neurons, which have a namesake ring-shaped morphology[32] and contact the whole suite of the HD neurons[33], just like the habenula axons. A subset of the ellipsoid body ring neurons have local visual receptive fields[34], and the experience-dependent plasticity between the ellipsoid body ring and E-PG establishes plastic anchoring of the landmarks to the head direction representation[5,6].

One of the more surprising observations here is that the symmetry in the visual scene leads to 'stretched' mapping from 180° of the visual space onto the 360° of the head direction (Fig. 4). Such drastic remapping is made possible by two factors: first, the all-to-all habenula-to-HD connectivity carries no intrinsic notion of retinotopy. This plastic, all-to-all connectivity resembles the 'parallel fibre system' motif, which can be found in various learning-related structures (for example, the cerebellum and insect mushroom body)[35]. Second, the strong inhibitory interactions among the HD neurons force the antipodic pairs of HD neurons to learn maximally dissimilar patterns of habenula inputs. Similar modes of contrastive learning guided by interactions among postsynaptic neurons have also been found in other parallel fibre systems[36].

In mammals, the three major brain regions containing the HD neurons are the lateral mammillary nucleus, the anterodorsal nucleus of the thalamus and the postsubiculum, which form a loop and maintain a coherent representation of heading[15,37]. The anchoring of the heading representation to visual landmarks is thought to happen through interactions between the retrosplenial cortex and postsubiculum[38,39], which is then propagated back to the subcortical areas through feedback projections[40]. By contrast, the observations of HD cells in the teleost forebrain are limited[41], and overall, the homology of mammalian thalamocortical connections in fish is questioned[42,43]. In light of the highly conserved nature of the habenula–IPN projection[20], our results suggest an evolutionary scenario in which the habenula–IPN mechanisms for landmark anchoring similar to those of insects first evolved in early vertebrates, and the forebrain circuitry was added on top of them, as the elaborate visual telencephalon evolved in mammals.

A key open question is the identities of AHV and rotation cells (Fig. 2b). We found cells in rhombomere 2/3 that exhibit visuomotor tuning with contingencies expected from AHV cells (Extended Data Fig. 10e–j), similar to fly GLNO cells[44]. From their position, we suspect these cells to be homologous to the rodent supragenual nucleus, which is considered to provide angular head velocity information to the DTN[45]. Furthermore, we do not yet know in which behavioural contexts fish utilize the head direction memory. Establishing a paradigm to observe behavioural manifestation of head direction memory is crucial to understand the outputs of the compass circuitry.

Online content

Any methods, additional references, Nature Portfolio reporting summaries, source data, extended data, supplementary information, acknowledgements, peer review information; details of author contributions and competing interests; and statements of data and code availability are available at https://doi.org/10.1038/s41586-025-09888-x.

1. Taube, J. S., Muller, R. U. & Ranck, J. B. Head-direction cells recorded from the postsubiculum in freely moving rats. II. Effects of environmental manipulations. *J. Neurosci.* **10**, 436–447 (1990).
2. Seelig, J. D. & Jayaraman, V. Neural dynamics for landmark orientation and angular path integration. *Nature* **521**, 186–191 (2015).
3. Petrucco, L. et al. Neural dynamics and architecture of the heading direction circuit in zebrafish. *Nat. Neurosci.* **26**, 765–773 (2023).
4. Aizawa, H. et al. Laterotopic representation of left-right information onto the dorso-ventral axis of a zebrafish midbrain target nucleus. *Curr. Biol.* **15**, 238–243 (2005).
5. Fisher, Y. E. et al. Sensorimotor experience remaps visual input to a heading-direction network. *Nature* **576**, 121–125 (2019).
6. Kim, S. S. et al. Generation of stable heading representations in diverse visual scenes. *Nature* **576**, 126–131 (2019).
7. Grieves, R. M. & Jeffery, K. J. The representation of space in the brain. *Behav. Process.* **135**, 113–131 (2017).
8. Taube, J. S., Muller, R. U. & Ranck, J. B. Head-direction cells recorded from the postsubiculum in freely moving rats. I. Description and quantitative analysis. *J. Neurosci.* **10**, 420–435 (1990).
9. Skaggs, W. E. et al. A model of the neural basis of the rat's sense of direction. *Adv. Neural Inf. Process. Syst.* **7**, 173–180 (1995).
10. Cullen, K. E. & Taube, J. S. Our sense of direction: progress, controversies and challenges. *Nat. Neurosci.* **20**, 1465–1473 (2017).
11. Puelles, L. Comments on the limits and internal structure of the mammalian midbrain. *Anatomy* **10**, 60–70 (2016).
12. Bassett, J. P. & Taube, J. S. Neural correlates for angular head velocity in the rat dorsal tegmental nucleus. *J. Neurosci.* **21**, 5740–5751 (2001).
13. Sharp, P. E., Tinkelman, A. & Cho, J. Angular velocity and head direction signals recorded from the dorsal tegmental nucleus of gudden in the rat: implications for path integration in the head direction cell circuit. *Behav. Neurosci.* **115**, 571–588 (2001).
14. Taube, J. S. et al. The head-direction signal is generated from two types of head direction cells in brainstem nuclei. *Nat. Commun.* **16**, 9755 (2025)
15. Yoder, R. M., Clark, B. J. & Taube, J. S. Origins of landmark encoding in the brain. *Trends Neurosci.* **34**, 561–571 (2011).
16. Creamer, M. S. et al. A flexible geometry for panoramic visual and optogenetic stimulation during behavior and physiology. *J. Neurosci. Methods* **323**, 48–55 (2019).
17. Chen, T.-W. W. et al. Ultrasensitive fluorescent proteins for imaging neuronal activity. *Nature* **499**, 295–300 (2013).
18. Förster, D. et al. Genetic targeting and anatomical registration of neuronal populations in the zebrafish brain with a new set of BAC transgenic tools. *Sci. Rep.* **7**, 5230 (2017).
19. Orger, M. B. et al. Perception of Fourier and non-Fourier motion by larval zebrafish. *Nat. Neurosci.* **3**, 1128–1133 (2000).
20. Aizawa, H., Amo, R. & Okamoto, H. Phylogeny and ontogeny of the habenular structure. *Front. Neurosci.* **5**, 138 (2011).
21. Dreosti, E. et al. Left-right asymmetry is required for the habenulae to respond to both visual and olfactory stimuli. *Curr. Biol.* **24**, 440–445 (2014).
22. Zhang, B. et al. Left habenula mediates light-preference behavior in zebrafish via an asymmetrical visual pathway. *Neuron* **93**, 914–928.e4 (2017).
23. Lavian, H. et al. Visual motion and landmark position align with heading direction in the zebrafish interpeduncular nucleus. *Nat. Commun.* **16**, 9924 (2025).
24. Bianco, I. H. et al. Brain asymmetry is encoded at the level of axon terminal morphology. *Neural Dev.* **3**, 9 (2008).
25. Wu, Y. K., Petrucco, L. & Portugues, R. Anatomical and functional organization of the interpeduncular nucleus in larval zebrafish. Preprint at *bioRxiv* https://doi.org/10.1101/2024.10.09.617353 (2024).
26. Satou, C. et al. Transgenic tools to characterize neuronal properties of discrete populations of zebrafish neurons. *Development* **140**, 3927–3931 (2013).
27. Brysch, C., Leyden, C. & Arrenberg, A. B. Functional architecture underlying binocular coordination of eye position and velocity in the larval zebrafish hindbrain. *BMC Biol.* **17**, 110 (2019).
28. Chen, X. et al. Brain-wide organization of neuronal activity and convergent sensorimotor transformations in larval zebrafish. *Neuron* **100**, 876–890.e5 (2018).
29. Feierstein, C. E. et al. Dimensionality reduction reveals separate translation and rotation populations in the zebrafish hindbrain. *Curr. Biol.* **33**, 3911–3925.e6 (2023).
30. Portugues, R. et al. Whole-brain activity maps reveal stereotyped, distributed networks for visuomotor behavior. *Neuron* **81**, 1328–1343 (2014).
31. Alexander, E. et al. Optic flow in the natural habitats of zebrafish supports spatial biases in visual self-motion estimation. *Curr. Biol.* **32**, 5008–5021.e8 (2022).
32. Hanesch, U., Fischbach, K.-F. & Heisenberg, M. Neuronal architecture of the central complex in *Drosophila melanogaster*. *Cell Tissue Res.* **257**, 343–366 (1989).
33. Hulse, B. K. et al. A connectome of the *Drosophila* central complex reveals network motifs suitable for flexible navigation and context-dependent action selection. *eLife* **10**, e66039 (2021).
34. Seelig, J. D. & Jayaraman, V. Feature detection and orientation tuning in the *Drosophila* central complex. *Nature* **503**, 262–266 (2013).
35. Cayco-gajic, N. A. & Silver, R. A. Review re-evaluating circuit mechanisms underlying pattern separation. *Neuron* **101**, 584–602 (2019).
36. Jacob, P. F. & Waddell, S. Spaced training forms complementary long-term memories of opposite valence in *Drosophila*. *Neuron* **106**, 977–991.e4 (2020).
37. Peyrache, A. et al. Internally organized mechanisms of the head direction sense. *Nat. Neurosci.* **18**, 569–575 (2015).
38. Clark, B. J. et al. Impaired head direction cell representation in the anterodorsal thalamus after lesions of the retrosplenial cortex. *J. Neurosci.* **30**, 5289–5302 (2010).
39. van der Goes, M.-S. H. et al. Coordinated head direction representations in mouse anterodorsal thalamic nucleus and retrosplenial cortex. *eLife* **13**, e82952 (2024).
40. Yoder, R. M., Peck, J. R. & Taube, J. S. Visual landmark information gains control of the head direction signal at the lateral mammillary nuclei. *J. Neurosci.* **35**, 1354–1367 (2015).
41. Vinepinsky, E. et al. Representation of edges, head direction, and swimming kinematics in the brain of freely-navigating fish. *Sci. Rep.* **10**, 14762 (2020).
42. Bloch, S. et al. Non-thalamic origin of zebrafish sensory nuclei implies convergent evolution of visual pathways in amniotes and teleosts. *eLife* **9**, e54945 (2020).
43. Mueller, T. What is the thalamus in zebrafish? *Front. Neurosci.* **6**, 64 (2012).
44. Hulse, B. K. et al. A rotational velocity estimate constructed through visuomotor competition updates the fly's neural compass. Preprint at *bioRxiv* https://doi.org/10.1101/2023.09.25.559373 (2023).
45. Graham, J. A. et al. Angular head velocity cells within brainstem nuclei projecting to the head direction circuit. *J. Neurosci.* **43**, 8403–8424 (2023).

Publisher's note Springer Nature remains neutral with regard to jurisdictional claims in published maps and institutional affiliations.

Open Access This article is licensed under a Creative Commons Attribution-NonCommercial-NoDerivatives 4.0 International License, which permits any non-commercial use, sharing, distribution and reproduction in any medium or format, as long as you give appropriate credit to the original author(s) and the source, provide a link to the Creative Commons licence, and indicate if you modified the licensed material. You do not have permission under this licence to share adapted material derived from this article or parts of it. The images or other third party material in this article are included in the article's Creative Commons licence, unless indicated otherwise in a credit line to the material. If material is not included in the article's Creative Commons licence and your intended use is not permitted by statutory regulation or exceeds the permitted use, you will need to obtain permission directly from the copyright holder. To view a copy of this licence, visit http://creativecommons.org/licenses/by-nc-nd/4.0/.

© The Author(s) 2026

Methods

Animal husbandry

The animal handling and experiments were performed according to protocols approved by the animal welfare officer at Institüt für Neurowissenschaften, Technische Universität München (TUM) and the relevant department at the regional government (Regierung von Oberbayern, Sachgebiet 55.2; animal protocol number 55-2-1-54-2532 10112 and 55.2-2532.Vet_02-24-5). Adult zebrafish (*Danio rerio*) were housed in the facility at the Institute for Neuronal Cell Biology at TUM. The adult fish were maintained in water temperature of 27.5–28.0 °C on the 14–10 h light–dark cycle. All experiments were performed on 6–9 days post-fertilization larvae of undetermined sex. The eggs were kept in 0.3× Danieau solution, and in the water from the fish facility upon hatching. The larvae were maintained at 28.0 °C and under the 14–10 h light–dark cycle.

Animal strains

All imaging experiments of the HD neurons were performed on fish carrying *Tg(gad1b-Gal4)mpn155* (ref. 18) and *Tg(UAS-GCaMP6s)mpn101* (ref. 46). To record the activity of habenula neurons (Extended Data Fig. 8), either *Tg(vglut2a-Gal4)nns20* (ref. 26) ($n = 6$ fish) or a previously uncharacterized enhancer trap line *Tg(18107-Gal4)* was used ($n = 2$ fish) with UAS-GCaMP6s. The expression pattern of the 18107-Gal4 line can be browed on Z Brain Atlas (https://zebrafishexplorer.zib.de/home/). For labelling habenula for the ablation (Fig. 5 and Extended Data Fig. 9), *Tg(18107-Gal4)* was used. A subset of fish in the ablation experiment possessed *Tg(UAS-nfsB-mCherry)*[47] for a logistical reason. This does not affect the results of the ablation experiments as they were evenly distributed across the conditions, and the fish were not treated with relevant chemogenetic reagents. The experiment to search for putative AHV cells (Extended Data Fig. 10e–j) was performed on fish carrying *Tg(HuC-H2B-jGCaMP7c)*. All fish were *mitfa*$^{-/-}$ (that is, nacre) mutants lacking melanophores to allow optical access to the brain.

Two-photon microscopy experiments

Animal preparation and the stimulus presentation setup. Animals were embedded in 2% low-melting point agarose in 30-mm petri dishes. The agarose around the tail was carefully removed with a scalpel to allow tail movements. The dish was mounted on a 3D-printed pedestal and placed in a cube-shaped acrylic tank with the outer edge length of 51 mm. The height of the pedestal was designed so that the head of the animal came to the centre of the tank, taking the thickness of the dish and the typical amount of agarose into account. The tank was then filled with fish facility water to minimize the refraction due to the petri dish wall. The three sides of the tank (except for the one facing the back of the fish) were made of single-side frosted acrylic (PLEXIGLAS Satinice 0M033 SC), which functioned as projection screens. The diffusive side faced inwards to minimize the reflections between the walls. The visual stimuli were projected onto the three walls through two sets of mirrors with a previously described geometry[16] (Supplementary Video 1), subtending 270° horizontally and 90° vertically. The larvae were lit with an infrared LED array through the transparent back wall of the tank. Their tail movements were monitored from below with a high-speed camera (Allied Vision Pike F032) at 200 Hz, through a hot mirror and a short pass filter to reject the excitation beam.

Microscope. Functional imaging was performed with a custom-built two-photon microscope. The excitation was provided by a femtosecond pulsed laser with 920-nm wavelength, the repetition rate of 80 MHz and the average source power of 1.8 W (Spark ALCOR 920-2). The average power at the sample was approximately 10 mW. The scan head consisted of a horizontally scanning 12-kHz resonant mirror and a vertically scanning galvo mirror, controlled by a FPGA running a custom LabView code (LabView 2015)[48]. Pixels were acquired at 20 MHz and averaged eightfold, resulting in the frame rate of 5 Hz. The typical dimension of the image was about 100 μm × 100 μm, with the resolution of about 0.2 μm per pixel. Only pixels corresponding to the middle 80% of the horizontal scanning range were acquired to avoid image distortion, and the area outside was not excited to minimize photo-damage. The fast power modulation was achieved with the acousto-optic modulator built in to the laser.

Stimulus protocols. All visual stimulus presentation and behavioural tracking were performed using Stytra package[49] (v0.8). The panoramic virtual reality environments were created and rendered using OpenGL through a Python wrapper (ModernGL). In each frame of the stimuli, three views of the virtual environment corresponding to the three screen walls were rendered, which were arranged on the projector window to fit the screens. Behavioural tracking was performed as previously reported[49]. In brief, seven to nine linear segments were fit to the tail of the larva, and the 'tail angle' was calculated at each camera frame as the cumulative sum of the angular offsets between the neighbouring pairs of segments. To detect swimming bouts, a running standard deviation of the tail angle within a 50-ms window was calculated ('vigour'). A swimming bout is defined as a contiguous period during which the vigour surpassed 0.1 rad. For each bout, the average tail angle within 70 ms after the onset was calculated, with a subtraction of the baseline angle 50 ms before the bout onset. This average angle ('bout bias') captures the first cycle of the tail oscillation in a bout and correlates well with the heading change in the freely swimming larvae[50]. We estimated the head direction of the fish in the virtual world as the cumulative sum of bout bias. The time trace of the head direction was also smoothed with a decaying exponential with the time constant of 50 ms, such that swim bouts result in smooth rotations of the scene (as opposed to instantaneous jumps).

For the recordings from the HD neurons, we simulated a virtual cylinder around the fish, whose height was determined so that the gaze angles to the top and bottom would be respectively ±60°. Various textures representing the visual scene, generated with the dimension of 720 × 240 pixel, were mapped onto this virtual cylinder. Dynamic aspects of the stimuli (that is, scene rotations and movements of the dots) were achieved by updating the textures on the cylinder. The visual scenes used were as follows:

- Flash: uniform fields of black or white.
- Sun-and-bars: three black vertical bars on a single radial gradient of luminance, ranging from white at the centre and black at the periphery. The bars were 15° wide and respectively centred at −90°, +75°,and +105° azimuths (0° is to the front and positive angles to the right). The centre of the gradient was in front and 45° above the horizon, and the radius was 135°.
- Translating dots: dots randomly distributed in a virtual 3D space at the density of 7.2 cm^{-3} moved at 10 mm s^{-1} sideways. The dots within the 40-mm cubic region around the observer were projected as 3 × 3-pixel white squares against a black background (in a texture bitmap on the cylinder), regardless of the distance.
- Stonehenge: four white vertical bars on a black background. The bars were positioned at −120°, −90°, 0° and +135° azimuths, respectively. The rightmost bar was broken in the vertical direction with the periodicity of 20° elevation and the duty cycle of 50%.
- Cue-cards: a white rectangle with the 90° centred about the 0° azimuth, which spanned the elevation ranges of either above +20° (top cue) or below −20° (bottom cue). The background was black.
- Noise: a 2D array of uniform random numbers within [0, 1], smoothed with a 5 × 5 pixel 2D boxcar kernel and binarized into black and white at 0.5.
- Single sun: a radial gradient of luminance from white at the centre and black at the periphery, centred at −90° azimuth and 35° above the horizon, with the radius of 60°.

- Double sun: the same as the single-sun scene, but symmetrized around the vertical meridian.

To identify and exclude naively visual neurons, each HD cell recording started with the alternating presentation of white and black flashes (8 s long each, five repetitions). In the experiment in Extended Data Fig. 3 the translating dots moving leftwards and rightwards alternatingly were also presented (8 s long, five repetitions). Afterwards, epochs of closed-loop scene presentations started. At the beginning of each epoch, the scene orientation was reset to 0°. On top of the closed-loop control, episodes of exogenous slow rotation (18° s^{-1}) were superimposed intermittently (5 s every 30 s (Figs. 1 and 2 and Extended Data Figs. 3 and 4a–g) or 20 s (Figs. 3–5 and Extended Data Fig. 4h–m)). The directions of the rotations flipped after every four rotational episodes. The structures of the virtual cylinder experiments were as follows:

- Sun-and-bars experiment (introduced in Fig. 1): in the first epoch (10 min), the sun-and-bars scene was presented. In the second epoch (10 min), fish received no visual stimuli (that is, darkness).
- Translating dots experiment (introduced in Extended Data Fig. 3): in the first epoch (8 min), the sun-and-bars ($n = 10$ fish) or Stonehenge ($n = 15$ fish) scene was presented. In the second epoch (15 min), the fish observed translating dots moving either left or right. The dots disappeared and the screen turned uniform white if the fish performed a bout or 10 s passed without a bout (that is, no rotational visual feedback). The dots reappeared after waiting for 10 s.
- Stonehenge experiment (introduced in Extended Data Fig. 4a–g): in the first and second epochs (8 min each), the sun-and-bars and the Stonehenge scenes were presented, respectively.
- Cue-card experiment (introduced in Extended Data Fig. 4h–m): the sun-and-bars, bottom cue-card and top cue-card scenes were presented for 4 min each.
- Jump and noise experiment (introduced in Fig. 2): in the first and second epochs (6 min each), the sun-and-bars scene was presented. In the second epoch, the superimposed exogenous rotations were swapped with abrupt 90° jumps. In the third epoch (6 min), the noise scene was presented.
- Symmetry experiment (introduced in Fig. 3): in the first and third epochs (12 min each), the single-sun scene was presented. In the second epoch (12 min), either the double-sun scene ($n = 25$ fish; Fig. 3) or single-sun scene ($n = 20$ fish; Extended Data Fig. 7) was presented.
- Ablation experiment (introduced in Fig. 5): in all epochs, the sun-and bars scene was presented. The first epochs were 12 min and 6 min long in the pre-ablation and post-ablation recordings, respectively. In the second epochs (6 min), the superimposed exogenous rotations were swapped with abrupt 90° jumps.

The experiment to characterize habenula visual responses (Extended Data Fig. 8) started with alternating black and white flash presentations (6 s each, five repetitions), which were used to select visually responsive cells. Next, white vertical or horizontal bars against a dark (25% luminance) background (which respectively subtended the entire height or circumference of the cylinder) were presented at 16 different azimuths and 5 different elevations, respectively. The width of the bar was 14°, and their azimuths and elevations were evenly spaced in the range of [−112.5° to 112.5°] and [−30° to 30°], respectively. Each presentation of bars lasted 4 s, with the interleave of 6 s. Each orientation and position combination were repeated three times, and the presentation order was randomized. Finally, the sun-and-bars scene rotating about the fish for the full 360° at 9° s^{-1} in an open loop was presented four times, in alternating directions. In the habenula ablation experiment, we recorded the responses of the habenula neurons to alternating black and white flash stimuli (8 s each, ten repetitions) to determine the visually responsive side (Extended Data Fig. 9b,c).

For the experiment to look for putative AHV cells (Extended Data Fig. 10e–j), we simulated a uniformly distributed point cloud in the 3D virtual reality environment (instead of simulating dots as a texture on the cylinder). Specifically, we simulated 2,000 dots within a cubic area with side length of 40 mm, and dots within the 20-mm radius from the observer were rendered as bright spots on a dark background with a diameter of about 1.2° (regardless of distance). Translational and rotational optic flow was simulated by moving the camera in the virtual environment. The experiment started with alternating presentations of short (5 s) yaw rotational optic flow and translational optic flow sideways, interleaved with 5 s of blank, dark screens, repeated five times, which were intended for characterizing the sensory responses of the cells. Next, leftwards and rightwards translational optic flow was continuously presented for 5 min each, which was intended to facilitate fish to turn, so that we could analyse the bout-triggered activity of the cells. The whole experiment was in open loop. The data acquired with two different sets of velocity parameters were merged together: in five fish, the speed of the rotational optic flow was 18° s^{-1}, and the translational optic flow moved 90° to the side at 5.0 mm s^{-1}. For the rest ($n = 16$ fish), the rotational optic flow was at 6° s^{-1}, and the translational optic flow moved 45° to the side-front at 3.0 mm s^{-1}.

Laser ablations. The habenula axons (that is, fasciculus retroflexus) were ablated unilaterally either by scanning a laser within a small region of interest (ROI) on the fasciculus retroflexus (setup A: Spectra Physics MaiTai, 830 nm, source power 1.5 W) or by pointing a laser on the fasciculus retroflexus (setup B: Spark ALCOR 920-2, 920 nm, source power 1.8 W). The pulsing characteristics of the two lasers were comparable (repetition rate of 80 MHz, pulse width of less than 100 fs), but ALCOR was group delay dispersion corrected and thus more efficient for ablations. On setup A, scanning with the duration of 200 ms was repeated 10 times with an interval of 300 ms. On setup B, a couple of approximately 100-ms-long pulses were delivered. These procedures were repeated until the successful ablation was confirmed either by a spot of increased fluorescence due to the photo-damage or a cavitation bubble. Ablations were repeated at two to three locations around the midbrain or pretectum levels to ensure the complete cut of the fasciculus retroflexus. The numbers of the fish treated on setups A and B were $n = 8$ and 8 (visual side ablated and control side, respectively) and 5 and 7 (visual side ablated and control side, respectively) fish, respectively. We waited at least 1 h after the ablation before making the post-ablation recordings.

Data analysis

Behavioural data analysis. The swim bouts estimated online during the experiments were analysed without additional preprocessing. In particular, we calculated trial-averaged cumulative turns around the exogenous scene rotations (Extended Data Fig. 1a,c,e–g), as well as comparing the biases of individual swim bouts with the scene orientation (Extended Data Fig. 1b,d).

Imaging data preprocessing. All imaging data were pre-processed using the suite2p package[51]. In brief, frames were iteratively aligned to reference frames randomly picked from the movie, using phase correlation. To detect ROIs representing cellular somata, a singular-value decomposition was performed on the aligned movie, and the ROIs were seeded from the peaks of the spatial singular-value vectors. All ROIs were used without morphological classifiers for cells, because the functional ROI selection procedure described below rejected spurious non-cell ROIs. In the ablation experiments, ROIs were manually defined, as described below.

ROI selection. For the HD neuron recordings, fluorescent time traces were first normalized into Z-scores for each ROI by subtracting the mean and dividing by the standard deviation. The normalized traces were then smoothed with a box-car kernel with the width of 1 s. Next, a scaled shifted sinusoid $a \times \cos(\theta - b) + c$ was fit to the smoothed traces of each ROI, where θ is the orientation of the visual scene relative to the fish. The fitting was performed with the 'curve_fit' function from the scipy package, and parameters were bounded in the range of $a \geq 0, b \in (-\pi, \pi]$. Only fractions of the data were used for this fitting to allow cross-validated quantifications of bump-to-scene alignments on the held-out fraction (described below). Specifically, either the second half of the first epoch (Figs. 1 and 3–5) or the entire first epoch (Fig. 2 and Extended Data Figs. 3 and 4) were used for fitting. ROIs with R^2 larger than 0.15 were considered to be sufficiently modulated by the scene orientation and included. In addition, pairwise Pearson correlations of response time traces to repeatedly presented flashes (and translating dots in Extended Data Fig. 3) at the beginning of the experiments were calculated for each ROI, and averaged across all pairs of repetitions. Naively visual ROIs with mean pairwise correlations above 0.1 were excluded from further analyses. Finally, rectangular masks were manually drawn around rhombomere 1 of the aHB, and the ROIs outside the mask were excluded.

For the habenula recordings (Extended Data Figs. 8 and 9), ROIs with mean pairwise correlations in response to repeated flashes (as described above) higher than 0.3 were selected as visually responsive ROIs and used for further analyses. For the putative AHV cell experiment (Extended Data Fig. 10e–j), for each ROI, we first calculated the mean pairwise correlations over the repeated presentation of short optic flows (two rotational and two translational directions, with interleaves). We selected ROIs that had a mean above 0.4 as reliable sensory ROIs. Next, for each sensory ROI for each presentation of short rotational optic flow, we normalized the fluorescence time trace $F(t)$ into $\frac{\Delta F}{F}(t) = \frac{F(t) - F_0}{F_0}$, where F_0 is the average fluorescence within the immediately preceding 3-s period during which no stimulus was presented. We then averaged this $\frac{\Delta F}{F}$ within the duration of each rotational optic flow presentation (that is, 5 s), and calculated the Z-scored directional difference

$$Z_{\text{dir}} = \frac{\mu_{\text{CW}} - \mu_{\text{CCW}}}{\sqrt{\frac{\sigma_{\text{CW}} + \sigma_{\text{CCW}}}{5}}},$$

where μ_d and σ_d are the mean and standard deviation, respectively, of the time-averaged normalized response over five repetitions ($d \in \{\text{CW}, \text{CCW}\}$ (in which CW denotes clockwise and CCW denotes anticlockwise); which is plotted in Extended Data Fig. 10f). ROIs with $|Z_{\text{dir}}| > 2$ were further analysed as rotation-direction-selective ROIs.

Ablation experiment-specific preprocessing. For each fish in the ablation experiment (Fig. 5), we first analysed the responses of the habenula neurons to the repeated flash stimuli. We first identified visually responsive ROIs as described above, and defined the side with more visual ROIs as the 'visual side'. In a minority of fish where the number of the visual ROIs from the two sides were close (within ±1 range), we determined the visual side based on morphology. This was possible due to the asymmetric expression of the 18107–Gal4. Overall, we found 3 fish with inverted laterality (that is, right visual) out of 28 included in the analysis (Extended Data Fig. 9c).

To compare the behaviours of the HD neurons before and after the fasciculus retroflexus ablations, ROIs were manually defined around the cells that were identifiable in both pre-ablation and post-ablation recordings. To minimize the effort for manual ROI drawing, we first used the ROIs detected by the suite2p pipeline from the pre-ablation recording, and run the HD cell selection procedure as described above. Using this as a guide, we drew manual ROIs on the pre-ablation recording, specifically focusing on the suite2p-based HD cell ROIs. We then calculated an affine transformation between the average frames of the pre-ablation and post-ablation recordings, and used this transform to register the manually defined ROIs to the post-ablation recordings. Finally, we manually adjusted the ROIs to better match the average post-ablation frames, if necessary. To make sure that we managed to identify the same cells across two recordings, we calculated the Pearson correlations of the smoothed fluorescence traces between all pairs of ROIs for each recording, and then computed the correlation of those correlations. We excluded fish with correlations of pairwise correlations below 0.4 from further analyses.

Characterization of HD tuning curves. To characterize the tuning of individual HD neurons, for each selected HD ROI, we calculated the average fluorescence binned according to the centred scene orientation $\theta(t) - b$ (Fig. 4a–f and Extended Data Figs. 2b,c, 7g and 9i,j), where b is the preferred scene orientation of the ROI. To assess the width of these tuning curves, we calculated the fraction of $\theta - b$ (that is, centred θ) bins where the response was above half maximum (Extended Data Fig. 2b,c).

For the data in the learning epoch of the symmetry experiment, we refit the tuning curves with scaled-shifted sinusoid with the single or double frequency. That is:

$$a' \times \cos(g(\theta - b) - b') + c',$$

where $g = 1$ (single frequency) or $g = 2$ (double frequency), and b' represents the tuning rotation in the learning epoch relative to the pre-learning epoch. Here we first compared the ROI-averaged R^2 from the $g = 1$ fits and $g = 2$ fits (Fig. 4b) to check whether the tuning curves were single or double peaked. We then compared the difference in b and b' for every pair of the HD cells in each recording, calculated the average of pairwise b' difference binned by b difference and estimated the slope between the two (Fig. 4c–f).

For the ablation data, we refit scaled-shifted sinusoid (with single frequency) for each epoch of each recording and compared the changes of R^2 before and after ablations, for each epoch type and each group (Extended Data Fig. 9i,j).

Bump phase calculation. As a readout of the population-level, instantaneous estimate of the scene orientation $\theta(t)$ by the HD neurons, we calculated the bump phase $\hat{\theta}(t)$, where t is discretized time. To do so, we first averaged the ROI-wise response time traces within eight 45° bins of the preferred orientation b. We excluded fish with more than four empty bins from the following analyses. We then computed the bump phase as:

$$\hat{\theta}(t) = \text{atan2}(y(t), x(t))$$

$$x(t) = \sum_i r_i(t)\cos b_i$$

$$y(t) = \sum_i r_i(t)\sin b_i,$$

where $r_i(t)$ is the average response of the i-th bin at time t, and b_i is the central angle of the i-th bin. The bump amplitude was also calculated as $A(t) = \sqrt{x(t)^2 + y(t)^2}$.

Scene–bump alignments. The alignment between the bump phase $\hat{\theta}$ and θ were examined in several different ways. First, we calculated the centred scene–bump offset $\Delta\theta(t) = [(\theta(t) - \hat{\theta}(t) + \pi)\text{mod}2\pi] - \pi$. For the cases where we can expect $\Delta\theta$ to be 0, we simply averaged absolute $\Delta\theta$ over time to obtain the 'absolute error' (AE) defined as $\text{AE} = \int |\Delta\theta| dt$. Second, when we expected $\Delta\theta$ to be non-zero but constant (that is, the bump follows the scene with an offset), we fit von Mises distribution $\left(\frac{e^{\kappa\cos(x-\mu)}}{\int e^{\kappa\cos x} dx}\right)$ to the histogram of $\Delta\theta$, where κ, a parameter that determines the peakiness of the distribution, can be interpreted as a proxy of how well the bump followed the scene. Third, in cases in which we expected the bump to follow the scene but with variable and non-unity gains (Fig. 2g), we calculated Pearson correlations between unwrapped $\theta(t)$ and $\hat{\theta}(t)$ within 15-s windows centred about the exogenous rotation episodes. We then calculated the median of these correlations over all rotation episodes, which we termed 'local correlation'. To more explicitly estimate the gain of visual-based and motor-based angular path integration, for each of the above 15-s snippets of unwrapped $\hat{\theta}(t)$, we performed a Ridge-regularized multiple regression by the exogenous component (that is, 90° rotation over 5 s) and the self-generated component (that is, the cumulative sum of bout biases) of $\theta(t)$. The Ridge regression was performed using scikit-learn 1.1.2 with $\alpha = 1$, and the regression coefficients (that is, the gain of path integration) were constrained to be non-negative. These metrics were also compared with various nuisance variables (Extended Data Fig. 1h–j).

In the translating dots experiment (Extended Data Fig. 3), the change in bout phase was correlated with, as well as regressed by, the bias of swim bouts. For each bout in the translating dots epoch, the change in the bump phase $\hat{\theta}$ was calculated as $\hat{\theta}(\tau + 5) - \hat{\theta}(\tau - 1)$, where τ is the bout onset (in seconds). For this calculation, we selected bouts that were separated by more than 5 s from both the preceding and the following bouts. A minority of bouts that had a bias of more than 120° and bouts in which tail tracking was faulty (tail not tracked in more than 10% of frames) were discarded as unreliable. Fish that did not have at least five such good bouts were excluded from the analysis. We had a single fish in the dataset that had two recordings that passed the above-quality thresholds. The correlations and slopes from multiple recordings in this fish were averaged.

Habenula visual responses. The visual receptive fields of habenula neurons were characterized as follows: first, for each ROI for each presentation of a bar, the fluorescence time trace $F(t)$ was normalized into $\frac{\Delta F}{F}(t) = \frac{F(t) - F_0}{F_0}$, where F_0 is the average fluorescence within the 2-s period immediately preceding the bar onset. The normalized responses were then averaged over repetitions for each orientation and position combination to generate the spatiotemporal receptive field maps as shown in Extended Data Fig. 8b, and averaged over time and divided by the peak response over positions to generate the normalized tuning curves in Extended Data Fig. 8c.

For the scene orientation decoding analysis, the responses of the visually responsive habenula ROIs were first concatenated across multiple recordings within each fish at different Z-depth. The response of each ROI was normalized into Z-scores for the entire recording (including the period during which the flashes and bars were presented; Extended Data Fig. 8d). Next, the normalized responses during the sun-and-bars scene presentation were downsampled to 1 Hz. For every pair of time points during the scene presentation (t_1, t_2), we calcualted the Pearson correlation between the pattern of habenula activities, which we denote as $r(t_1, t_2)$ (Extended Data Fig. 8e). For each time point during the scene presentation t, the decoded scene orientation was defined as:

$$\widetilde{\theta}(t) = \theta(t_{\max}),$$

$$t_{\max} = \mathrm{argmax}_{\tau}\{r(t, \tau) | \tau \in [0, 40]\}.$$

For each fish, we calculated the absolute error $\mathrm{AE}_{\mathrm{decode}} = \int_{40}^{160} |\theta(t) - \widetilde{\theta}(t)| dt$ to assess the quality of decoding.

Characterization of the putative AHV cells. To assess the anatomical distribution of the putative AHV cells, we mapped each recording into a common reference frame as follows: for each fish, alongside the planar functional recordings, we acquired a 1-µm or 2-µm step Z-stacks. First, we mapped the aligned, time-averaged frame of each functional recording onto the corresponding Z-stack with a manually defined key point-based affine transformation. Next, we mapped each Z-stack onto a single select Z-stack in the same way. This Z-stack-to-Z-stack mapping was performed separately for the groups of recordings targeted at rostral and caudal hindbrain regions. Then, we averaged the mapped Z-stacks across fish within the rostral and caudal groups. Finally, we mapped the average rostral stack onto the average caudal stack, exploiting the overlap between the two. The coordinates of all ROIs from all recordings in all fish were then linearly transformed into the average caudal stack coordinate with multistep affine transformations.

The bout-triggered activities of the rotation-direction-selective cells identified in the putative AHV cell experiment (Extended Data Fig. 10e–j) were characterized as follows: for each recording, we first identified turning swim bouts during the longer presentation of translational optic flows, which had the absolute bias above 0.2 rad. Recordings that did not have at least three turning bouts in both directions were excluded from further analyses. Next, for each ROI for each bout, we cut out a fluorescent snippet around the bout onset, and normalized it into $\frac{\Delta F}{F}(t) = \frac{F(t) - F_0}{F_0}$, where F_0 is the average fluorescence within the immediately preceding 3-s period. The normalized bout-triggered snippet was averaged within 3 s from the bout onset and averaged across bouts for each direction. We then calculated the difference of time-averaged and bout-averaged bout-triggered activity by turn directions, as plotted in Extended Data Fig. 10g. To assess the contingency of visual and motor directional preferences, for each ROI, we calculated the product between the Z-scored rotational optic flow response differences (Z_{dir}) and the directional differences of the bout-triggered responses (Extended Data Fig. 10h). This visuomotor product was averaged across cells within bins along the anteroposterior axis for each fish.

Statistical quantifications. As a rule, when comparing fish-wise metrics against null hypothesis values, or when making paired comparisons between different conditions within fish, we used the signed-rank tests. When comparing scalar metrics across two groups of fish, we used the rank-sum tests. To assess the significance of the alignment between the scene orientation $\theta(t)$ and the bump phase $\hat{\theta}(t)$ for each recording (more specifically, to show that the observed scene–bump alignment did not simply result from the autocorrelation of θ and $\hat{\theta}$), we used bootstrap tests with time-domain shifting, as follows: first, we calculated a metric of interest that quantifies the scene–bump alignment as $F_{\mathrm{data}} = F(\theta(t), \hat{\theta}(t))$. We then circularly shifted the bump phase $\hat{\theta}$ by a random amount Δt and recalculated the bootstrap metric $F_{\mathrm{BS}} = F(\theta(t), \hat{\theta}([t + \Delta t] \bmod T))$ for 1,000 times, where T is the duration of the relevant epoch or the experiment. We then calculated the probability of obtaining a value more extreme than F_{data} in the expected direction from the resampled distribution F_{BS} as the estimate of the statistical significance (that is, bootstrap P value) of the observation. Thus, the bootstrap tests were one-sided. When $F(\theta, \hat{\theta})$ depended on the temporal structure of θ and $\hat{\theta}$ (that is, local correlation and regression), care was taken such that the data snippets containing discontinuous points introduced by the circular shifting were not used for the F_{BS} calculation. To make sure that the observed significant fish-wise P values did not simply result by chance in the absence of true bump–scene alignments (that is, multiple comparison problem), we performed Kolmogorov–Smirnov tests to compare the observed P value distribution with a uniform distribution.

The specific statistical tests we performed, as well as the experiment specific exclusion criteria, are as follows:

- Sun-and-bars experiment: the absolute error $\mathrm{AE} = \int |\Delta\theta| dt$ was calculated for the hold-out (that is, not used for the HD cell identification) portion of the data, and its significance was tested with the bootstrap test (Fig. 1e and Extended Data Fig. 2e).
- Translating dots experiment: the correlation between the bout phase change across swim bouts and the bias of the swim bouts was tested against 0 with a signed-rank test (Extended Data Fig. 3f).
- Stonehenge experiment: von Mises distributions were fit on the histogram of $\Delta\theta$ (with 16 evenly spaced bins) in the Stonehenge epoch, and κ was tested with the bootstrap test (Extended Data Fig. 4d,g).
- Cue-card experiment: von Mises distributions were fit on the histogram of $\Delta\theta$ in the bottom and top cue epochs, and κ was tested with

the bootstrap test (Extended Data Fig. 4k,m). In addition, κ was compared across epochs within each recording with a signed-rank test (Extended Data Fig. 4l).

- Jump and noise experiment: von Mises distributions were fit on the histogram of $\Delta\theta$ in the jump and noise epochs, and κ was tested with the bootstrap test (Fig. 2f and Extended Data Fig. 5b,c). In addition, local correlation (Fig. 2h and Extended Data Fig. 5b,c), as well as trial-averaged R^2 from the multiple regression model (Fig. 2f and Extended Data Fig. 5e–g) were calculated on the noise epoch data and tested with the bootstrap test.
- Symmetry experiment: several fish whose bump amplitude A decayed more than 60% between the pre-training and post-training epoch (for example, owing to poor health) were discarded as unreliable. The 'fraction out-phase', that is, the proportion of time where $|\Delta\theta| > \frac{3\pi}{4}$ was calculated for each epoch (only using the hold-out part) and compared across epochs with signed-rank tests, separately for the double-sun (Fig. 3e) and control (Extended Data Fig. 7d) groups. The change in the fraction out-phase from the pre-learning to the post-learning epoch was compared across groups with a rank-sum test (Extended Data Fig. 7e). In Fig. 4b, ROI-averaged R^2 from single-frequency and double-frequency sinusoidal fits on the individual HD cell tuning curves in the learning epoch were tested against each other with a signed-rank test. In Fig. 4f, the slope between the pairwise tuning difference and the tuning rotation difference was tested against 0 with a signed-rank test. In Fig. 4i, von Mises distributions were fit on the histogram of $2\theta - \hat{\theta}$, and κ was tested with the bootstrap test (Extended Data Fig. 7h).
- Habenula experiment: the absolute error of decoding was tested against $\frac{\pi}{2}$ with a signed rank test (Extended Data Fig. 8f).
- Ablation experiment: von Mises distributions were fit on the histogram of $\Delta\theta$ for each epoch in each recording. We then compared the κ across the ablation group within each epoch of each recording with signed-rank tests (Fig. 5e). In addition, the ratios of κ between pre-ablation and post-ablation recordings for each epoch were compared across the ablation groups, using the rank-sum test (Fig. 5f). We excluded fish that had $\kappa < 0.5$in the pre-ablation epochs, as they were not informative about the effect of the ablations. In addition, visuomotor multiple regression models were fit to the bump-phase changes in the smooth epoch of the post-ablation recordings in the visual-side-ablated animals, and R^2 was tested with the bootstrap test (Extended Data Fig. 10c,d). We also tested the amount of stabilization turns fish made before and after ablations for each epoch–group combination, with signed rank tests (Extended Data Fig. 1g).
- Putative AHV cell experiment: the binned-averaged visuomotor product was tested against 0 for each anteroposterior bin, with signed-rank tests (Extended Data Fig. 10i).

Reporting summary

Further information on research design is available in the Nature Portfolio Reporting Summary linked to this article.

Data availability

The physiological, behavioural and anatomical data necessary to reproduce the figures have been deposited in a Zenodo repository[52] (https://doi.org/10.5281/zenodo.17233579). The expression pattern of the 181017–Gal4 driver line is available from the Z Brain Atlas (https://zebrafishexplorer.zib.de/home/).

Code availability

The code to analyse the deposited data is available from our Github repository (https://github.com/portugueslab/Tanaka_2025_landmark).

46. Thiele, T. R., Donovan, J. C. & Baier, H. Descending control of swim posture by a midbrain nucleus in zebrafish. *Neuron* **83**, 679–691 (2014).
47. Davison, J. M. et al. Transactivation from Gal4-VP16 transgenic insertions for tissue-specific cell labeling and ablation in zebrafish. *Dev. Biol.* **304**, 811–824 (2007).
48. Varga, Z. et al. Dendritic coding of multiple sensory inputs in single cortical neurons in vivo. *Proc. Natl Acad. Sci. USA* **108**, 15420–15425 (2011).
49. Štih, V. et al. Stytra: an open-source, integrated system for stimulation, tracking and closed-loop behavioral experiments. *PLoS Comput. Biol.* **15**, e1006699 (2019).
50. Huang, K. H. et al. Spinal projection neurons control turning behaviors in zebrafish. *Curr. Biol.* **23**, 1566–1573 (2013).
51. Pachitariu, M. et al. Suite2p: beyond 10,000 neurons with standard two-photon microscopy. Preprint at *bioRxiv* https://doi.org/10.1101/061507 (2017).
52. Tanaka, R. & Portugues, R. Dataset for "Plastic landmark anchoring in zebrafish compass neurons". *Zenodo* https://doi.org/10.5281/zenodo.17233579 (2025).

Acknowledgements We thank the members of the Portugues laboratory for constructive discussions on the project; M. Haesemeyer for the *Tg(18107–Gal4)* line; and K. Briggman for the *Tg(HuC–H2B–jGCaMP7c)* line. R.T. was supported by the European Molecular Biology Organization (EMBO ALTF 732-2022) and the Human Frontier Science Program (HFSP LT0027/2023-L) for this work. This research was funded by the German Research Foundation (DFG) under the Germany's Excellence Strategy within the framework of the Munich Cluster for Systems Neurology (EXC 2145 SyNergy, identifier 390857198), through the 'Enhanced resolution microscopy' project DFG – Projektnummer 518284373, by the Volkswagen Stiftung via a Life? grant and by the Max Planck Gesellschaft.

Author contributions R.T. and R.P. conceived the project. R.T. designed the virtual reality setup, performed the experiments and analysed the data. R.T. and R.P. wrote the manuscript.

Competing interests The authors declare no competing interest.

Additional information

Supplementary information The online version contains supplementary material available at https://doi.org/10.1038/s41586-025-09888-x.

Correspondence and requests for materials should be addressed to Ryosuke Tanaka or Ruben Portugues.

Peer review information *Nature* thanks the anonymous reviewer(s) for their contribution to the peer review of this work.

Reprints and permissions information is available at http://www.nature.com/reprints.

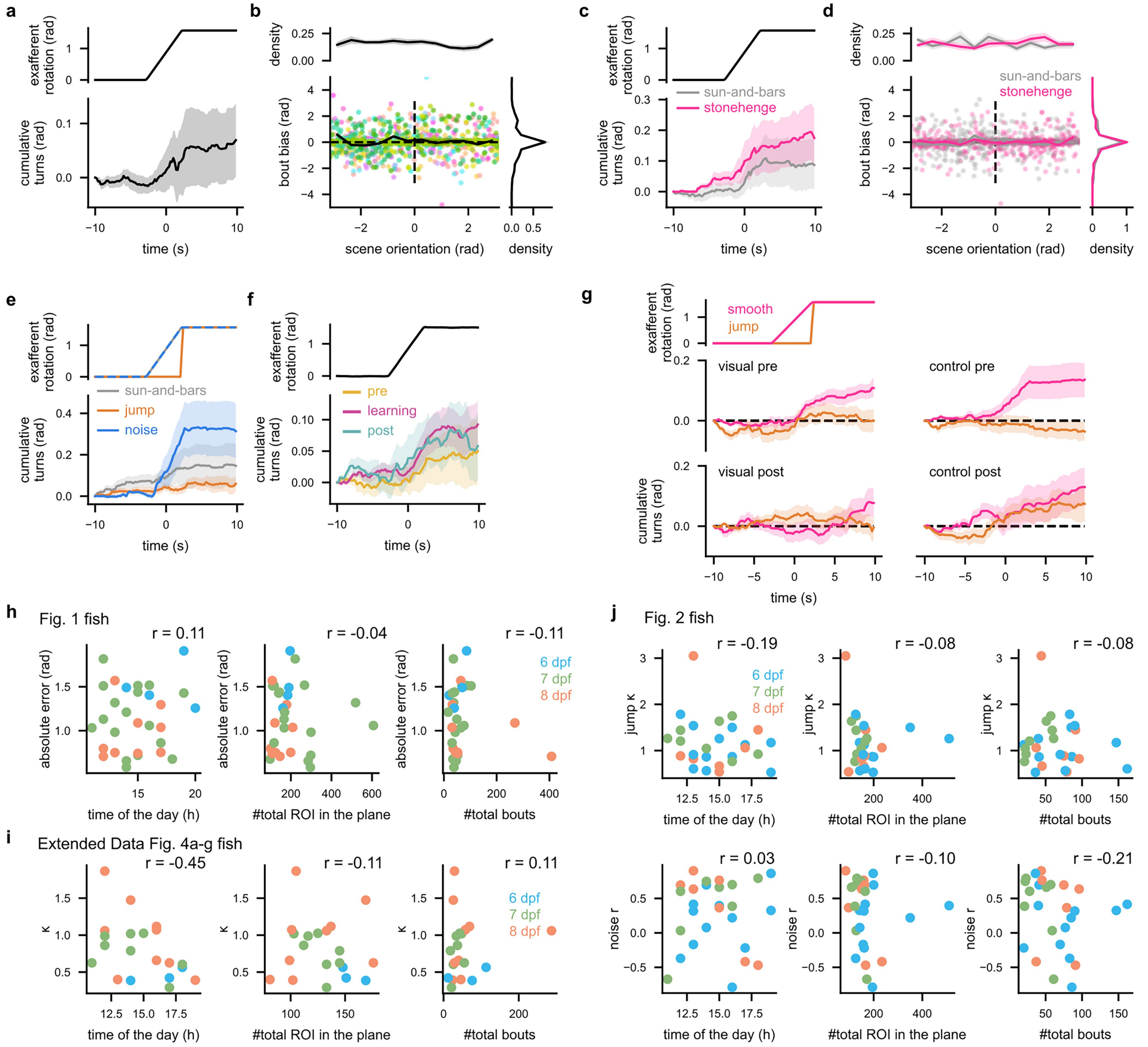

Extended Data Fig. 1 | Behaviors of the fish during the experiments and analyses of neural variability. (**a**) (*top*) The exafferent component of the scene rotation in the experiment in Fig. 1. (*bottom*) The cumulative turns fish made. The solid lines in (a-g) indicate the mean across fish, and the shaded area represents the standard error around it. The data are folded across clockwise and counterclockwise rotation episodes such that the exafferent rotation of the scene is always positive. Note that positive turns move the scene orientation negatively. (**b**) The bias of swim bouts, plotted against the scene orientation, in the experiment in Fig. 1 (i.e., with the sun and bars scene). The dots of the same color are from the same fish. The marginal distributions of the bout bias and the scene orientation is plotted above and to the side. If fish were consistently fixating on a specific part of the scene (e.g., the sun at the center), one would expect an N-shaped curve for the bias distribution. (**c, d**) The same as (a, b), but for the experiment in Extended Data Fig. 4a–g. (**e**) The same as (a), but for the experiment in Fig. 2. (**f**) The same as (a), but for the experiment in Figs. 3 and 4. Only the fish that experienced the double-sun scene are included. (**g**) The same as (a), but for the ablation experiment in Fig. 5, plotted separately for the groups, epoch types, and pre-/post-ablation recordings. We did not detect any significant difference in the amount fish turned in smooth epochs (i.e., endpoints of each curve at 10 s) across groups within recording types (pre p = 0.54; post p = 0.17) or before and after the ablations (visual p = 0.59; control p = 0.71). (**h**) The absolute error (AE) metric from Fig. 1, plotted against potential sources of variability (time of the day, the number of ROIs per plane, and the number of swim bouts). The larvae with different ages are color-coded. The Pearson correlation between the AE and the other variables are noted above the plots. We did not find any of the nuisance variables to be strongly correlated with the AE metric. (**i**) Same as (h), but for the κ metric for the Stonehenge epoch in the Extended Data Fig. 4a–g. (**j**) Same as (h, i), but for (*top*) the κ metric for the Jump epoch and (*bottom*) for the local correlation (r) from the Noise epoch in Fig. 2. Overall, we did not find a particularly consistent relationship between the scene tracking performance and the nuisance variables we had a handle on. Remaining plausible sources of the variability include the stochasticity in the expression pattern of the gad1b:Gal4 line, as well as the embedding condition of the animals (e.g., small tilt in the pitch or roll direction affected the HD neurons through the vestibular systems). (a, b, h) N = 25 fish. (c, d, i) N = 20 fish. (e, j) N = 24 fish. (f) N = 25 fish. (g) N = 13/15 fish (visual side/control) for the smooth epoch, and N = 12/13 (visual side/control) for the jump epoch. P-values are from rank-sum (for across fish comparisons) or signed-rank (for within fish comparisons) tests.

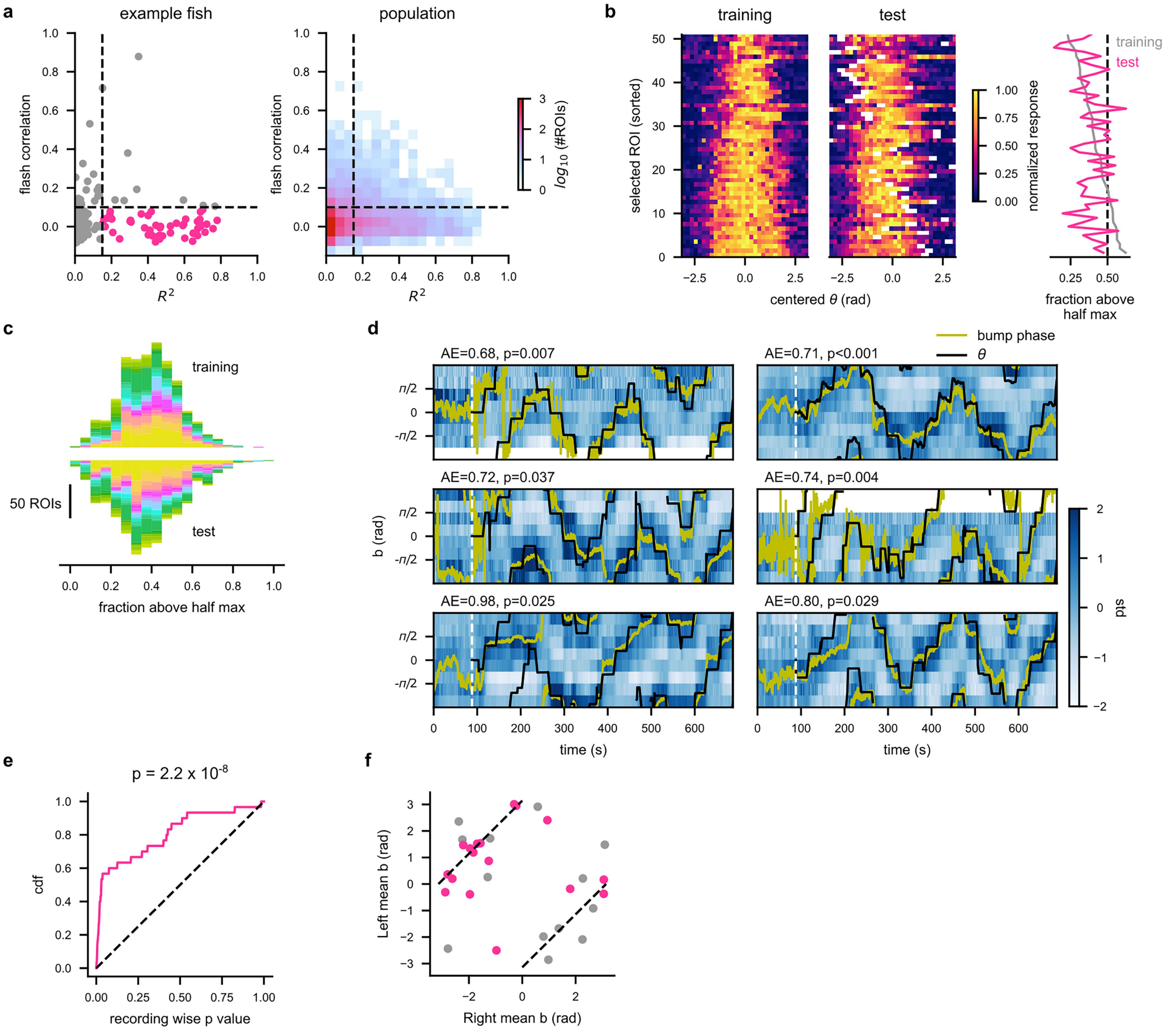

Extended Data Fig. 2 | Further characterizations of the scene orientation tuned cells in the Sun-and-bars scene. (**a**) (*left*) The distribution of the R^2 values from the sinusoidal fits and the mean pairwise correlation to the flash stimuli, for the same fish as in Fig. 1d and (*right*) for the population. (**b**) The normalized scene orientation tuning of selected individual ROIs, from the same fish in (a). Plotted separately for the portion used for the fitting ("training", *left*) and the portion not used ("test", *middle*). The ROIs are sorted by the tuning width proxyed by the fraction above half max from the training portion, as plotted on the right. (**c**) The distributions of the fraction above half max. Each color represents ROIs from different fish. On average, the scene orientation tuning of these cells were on average slightly narrower than the sinusoid. (**d**) The binned activity of the scene orientation tuned cells from six more example fish as in Fig. 1d. The dotted line marks the beginning of the Sun-and-bars scene. (**e**) The cumulative distribution of the recording-wise p-values from the bootstrap tests in Fig. 1e (pink), which was significantly ($p = 2.2 \times 10^{-8}$) different from the uniform distribution (black dotted), from a Kolmogorov-Smirnov test. (**f**) Mean preferred scene orientations b of the ROIs in the left and right hemispheres, plotted against each other. Pink dots are for the recordings where the absolute error was significantly below chance. The data roughly lay on top on the diagonal dotted lines indicating (left mean − right mean) = π. N = 30 recordings from 25 fish.

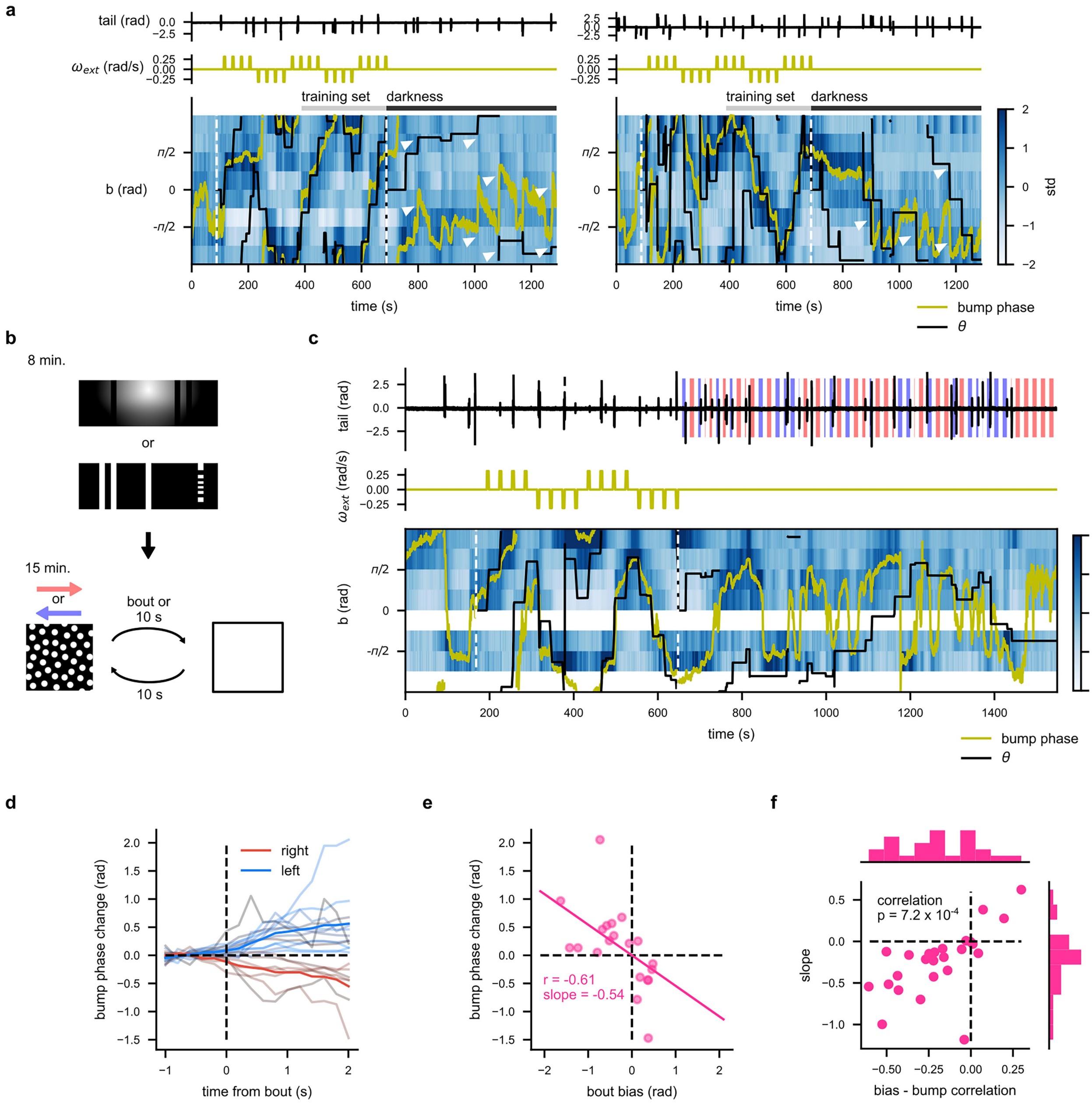

Extended Data Fig. 3 | Turns triggered by translational optic flow move the bump phase. (**a**) Binned activities of the scene orientation tuned cells from two example fish throughout the entire recording, as in Fig. 1d. The dotted white lines indicate the beginnings of the Sun-and-bars and darkness epochs, respectively. Places where lateralized swim bouts in the darkness appeared to coincide with bump phase changes are marked by white triangles. (**b**) Schematics of the experimental structure. (**c**) The binned activity of the scene orientation-tuned cells in an example fish, with the bump phase (yellow) and scene orientation *θ* (black) (note that *θ* did not correspond to the stimuli presented in the second epoch). The red and blue boxes on the tail plot respectively indicate periods during which rightward and leftward dots were presented. (**d**) The changes in the bump phase around each swim bout (thin lines). Thick lines are the averages for the right and left bouts (defined as bias > 0.2 and < −0.2 rad, respectively). (**e**) The bump phase change (i.e., average bump phase between 1 to 2 s after the bout onset, with a baseline subtraction) plotted against the bout bias. (**f**) The correlation and slopes between the bump phase change and bout bias distributions, plotted against each other. The histograms show the marginal distributions. The bout bias-bump phase change correlation was significantly negative across the population ($p = 7.2 \times 10^{-4}$ from a signed-rank test, N = 25 fish).

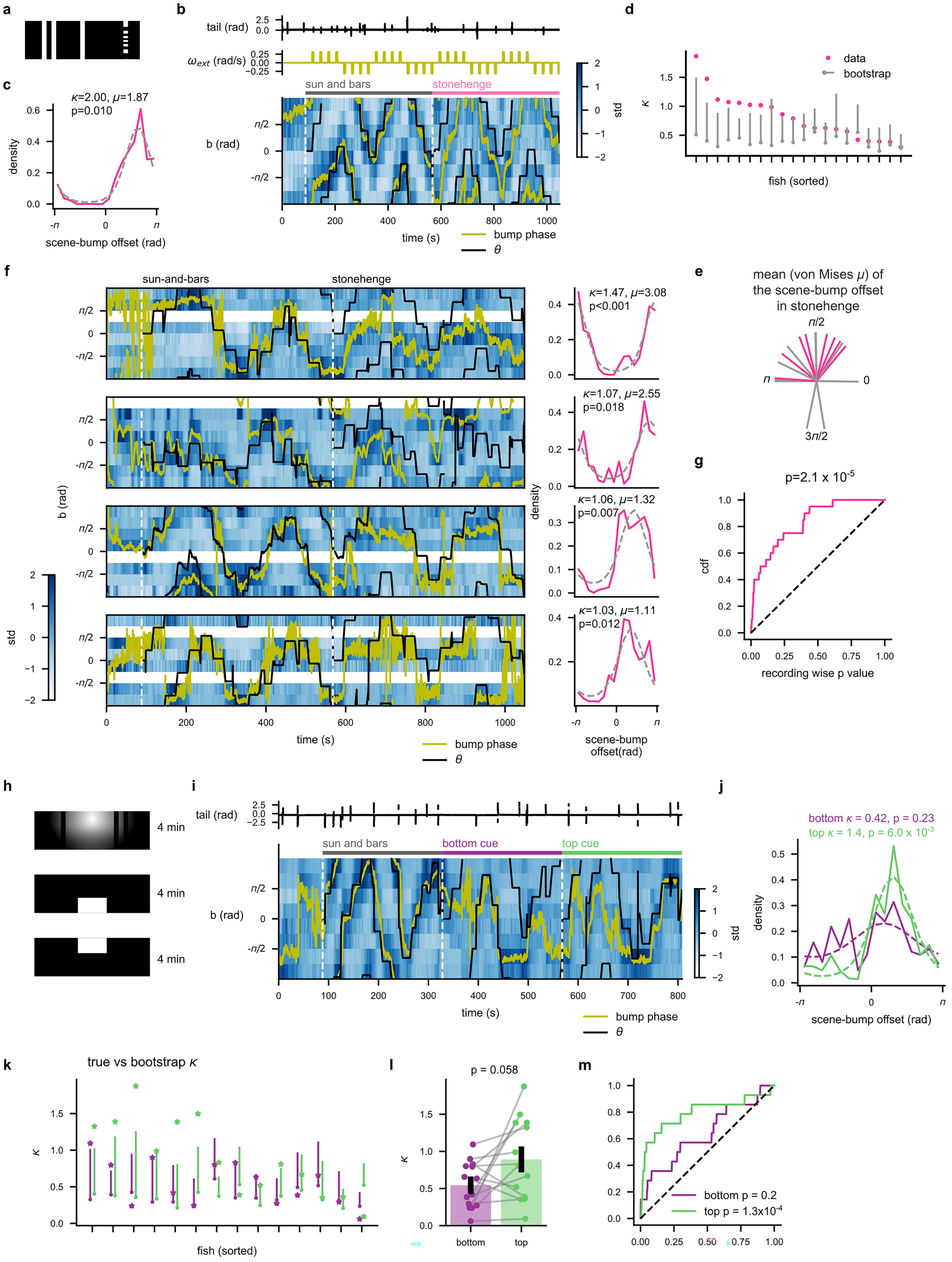

Extended Data Fig. 4 | See next page for caption.

Extended Data Fig. 4 | The HD neurons can track multiple scenes. (**a**) The Sun-and-bars scene (*top*) and the Stonehenge scene (*bottom*) were presented in sequence. (**b**) The data from an example fish, showing the (*top*) tail angle, (*middle*) exogenous rotation velocity ω_{ext}, and (*bottom*) the binned HD cell activity with the scene orientation θ (black) and the bump phase (yellow). (**c**) Histogram of the offset between θ and the bump phase during the Stonehenge epoch (pink), with a von Mises distribution fit to the data (grey dotted), which is proportional to $\exp(\kappa\cos(\theta-\mu))$. The p-value is from a bootstrap test and represents the probability that the κ is greater than the shuffle (see Methods). (**d**) κ from the von Mises distributions fit on the scene-bump offset histogram for each fish (pink), with the associated shuffle distribution (grey dot for the median, the bar for the 95th-percentile). 8 out of 20 fish showed significantly above chance κ. (**e**) The mean angle (μ) of the von Mises distribution fit on the scene-to-bump offset during the Stonehenge epoch. Pink lines represent the data from fish with significant κ. (**f**) Same as (b, c), but for more example fish. The p-values are from bootstrap tests on κ, as in (c). (**g**) The cumulative distribution of the p-values from the bootstrap tests on the von Mises κ (pink) shown in (d), which was significantly ($p = 2.1\times10^{-5}$) different from the uniform distribution (black dotted), from a Kolmogorov-Smirnov test. (**h**) To test if the elevation of the visual landmarks affects the HD cell behavior, we presented the fish with the same sun-and-bars scene (*top*), a scene with a bottom cue (*middle*), and a scene with a top cue (*bottom*). Each scene was presented for 4 min in a closed loop, with intermittent exogenous rotations. The HD cells were detected using the sun-and-bars epoch with the sinusoidal fitting procedure. (**i**) Binned activity of the HD cells and associated tail traces (*top*) from an example fish. The scene orientation θ (black) and the bump phase (yellow) are overlaid. (**j**) The histogram of the scene orientation-bump phase offset for bottom (purple) and top (green) cue epochs, with von Mises fits (dotted lines), from the same fish as in (i). The p-values are from bootstrap tests on κ, as in (c). (**k**) κ from the von Mises distributions fit on the scene-bump offset histogram for each fish (stars), with the associated shuffle distribution (dots for the median, the bar for the 95-percentile). Purple and green respectively indicate bottom- and top-cue epochs. (**l**) The distributions of bottom- and top-cue epoch κ across the whole population. The difference between two distributions was not significant, from a signed-rank test. The bars and error bars indicate the means across fish and their standard errors, respectively. The data points from the same fish are connected. (**m**) The cumulative distributions of the p-values for the von Mises κ from bootstrap tests, separately plotted for the bottom- and top-cue epochs. The p-values from the top-cue epochs were significantly below chance (i.e., uniform), from Kolmogorov-Smirnov tests. (d, g) N = 20 fish. (k, l, m) N = 12 fish.

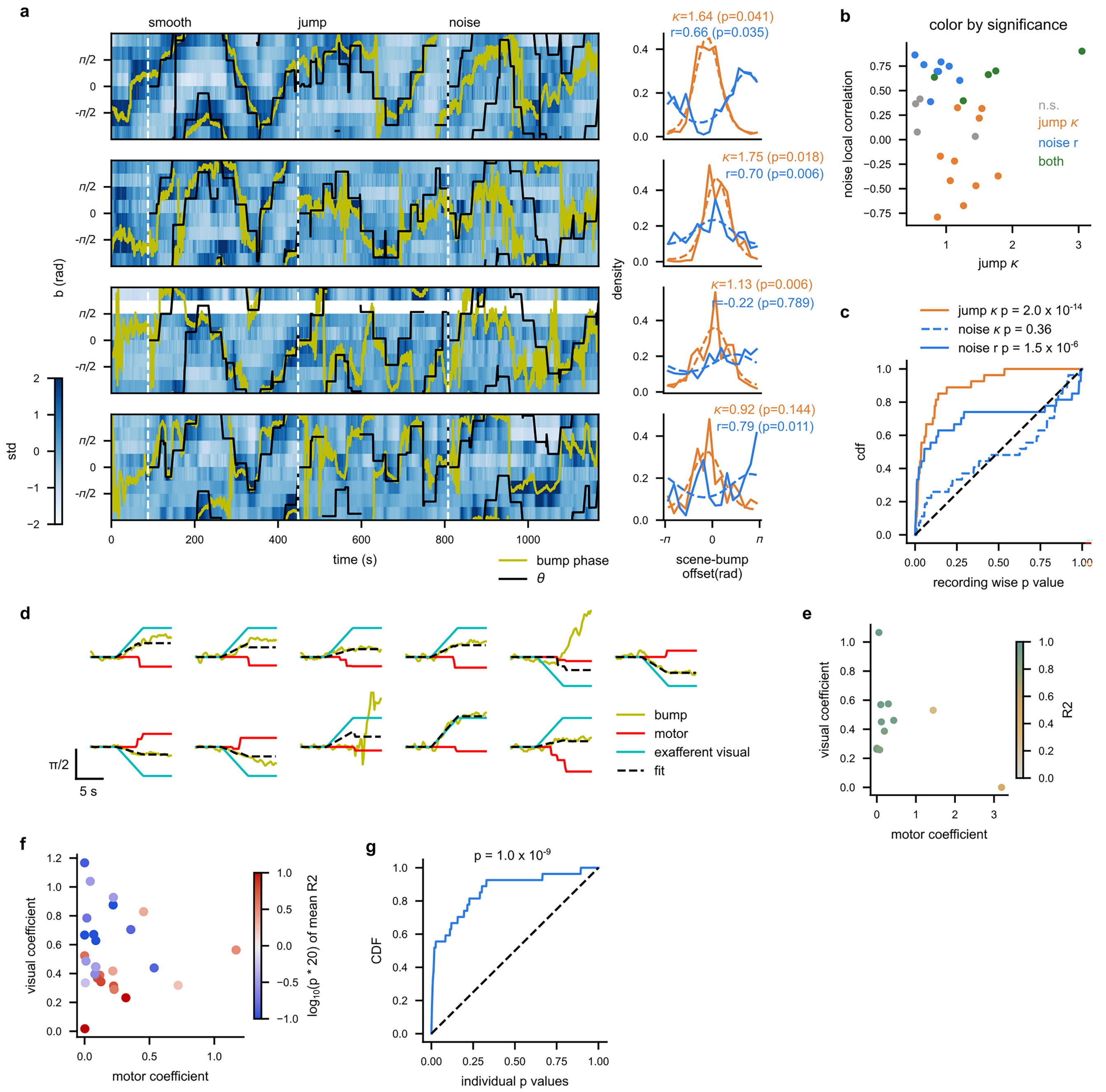

Extended Data Fig. 5 | Additional characterizations of landmark- and optic flow-based scene tracking by the HD neurons. (**a**) Binned activities of HD cells with bump phase and θ overlaid (*left*) and the associated histograms of the scene orientation-to-bump phase offsets (*right*) from more example recordings, as in Fig. 2d,e. The orange and blue solid lines respectively represent the Jump and Noise epochs, and dotted lines the von Mises distributions fit on them. The p-values are from bootstrap tests on κ and local correlation (see Methods). (**b**) The von Mises κ for the Jump epoch plotted against the local correlation in the Noise epoch for each recording, color-coded by the statistical significance of the two metrics. Out of 27 recordings, 5 showed both significant Jump epoch κ and Noise epoch correlation (green), 10 showed only significant κ (orange), 8 showed only significant correlation (blue), and 4 neither (grey). The significance is defined as bootstrap p values below 0.05. (**c**) The cumulative distribution of the p-values from the bootstrap test on the von Mises κ fit on the scene-bump offset histogram of the Jump (orange) and Noise (blue dotted) epochs, as well as on the local correlation between the bump phase and scene orientation (blue solid). The distributions of the p-values were significantly different from the uniform distribution (black dotted), except for the Noise κ, from Kolmogorov-Smirnov tests. (**d**) To independently estimate the gain of motor-based and optic flow-based angular path integration, the change in the bump phase (yellow) in the Noise epoch was regressed by the cumulative turn angles (motor, red) and cumulative exafferent visual rotation (exafferent visual, cyan). The fit was performed separately for each short (15 s) period around the exafferent rotation, with a Ridge regularization. The black dotted lines indicate the resultant fits. The data is from the same fish as in Fig. 2d. (**e**) The visual and motor coefficients plotted against each other, from the fits in (d). Each dot corresponds to each rotation episode. (**f**) The mean visual and motor coefficients averaged across rotation episodes within each fish, plotted against each other. Each dot represents a single recording, where colors indicate the p-value from bootstrap tests on the episode-averaged R^2 value (*Methods*). The colors are scaled with $\log_{10}(20*p)$, so that dots with $p < 0.05$ appear blue. (**g**) Same as (c), but for the p-value on the mean R^2 value of the regression models. The Kolmogorov-Smirnov test indicates that the distribution of the p-values is significantly different from uniform. N = 27 recordings from 24 fish.

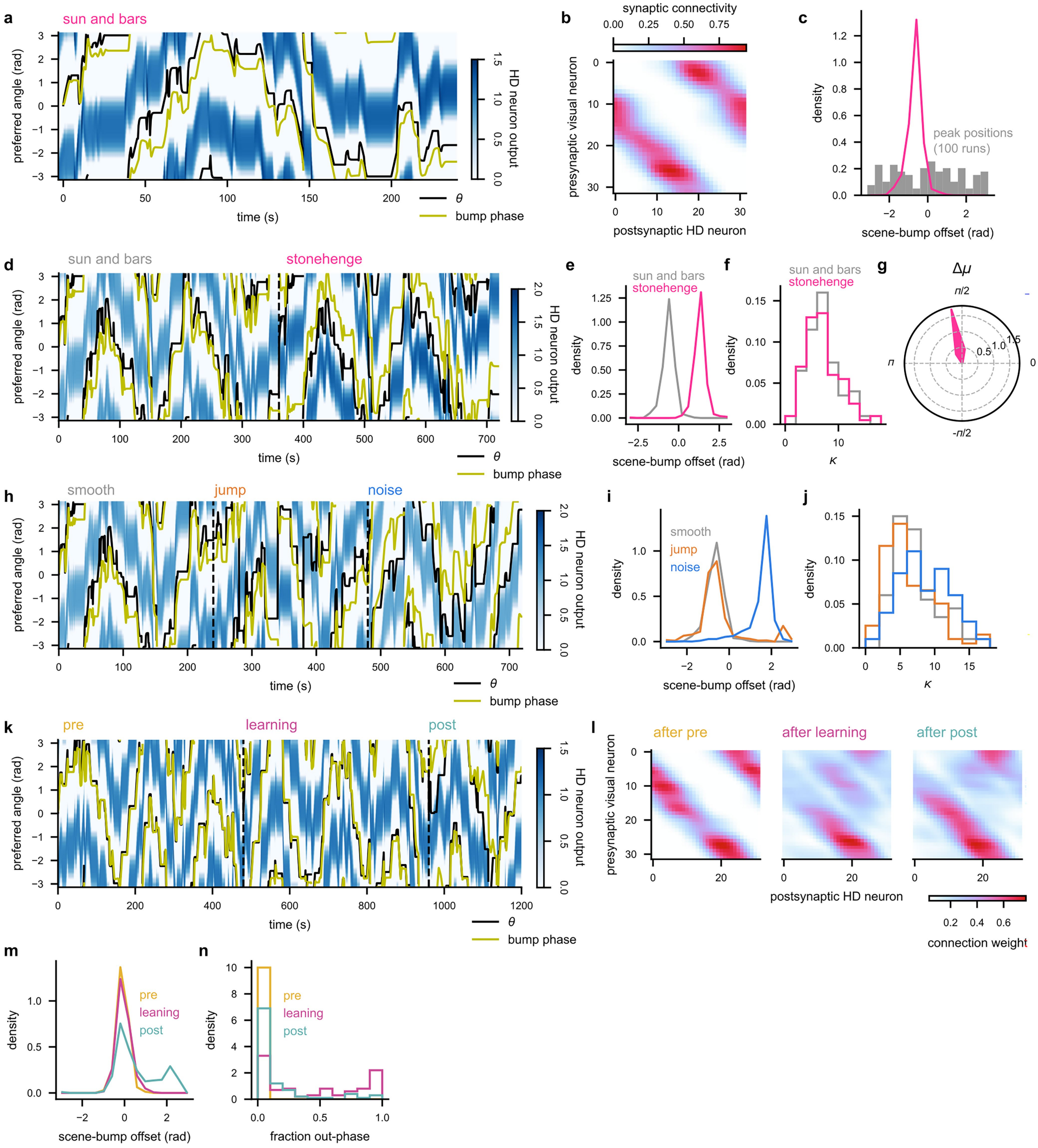

Extended Data Fig. 6 | See next page for caption.

Extended Data Fig. 6 | A simple ring attractor model with plastic visual inputs replicates the physiological observations. Please see Supplementary Note 1 for the details of the model implementation and the calibration procedure. (**a**) The outputs of model HD cells in a simulated experiment similar to Fig. 1, where the sun-and-bars scene was presented. The scene orientation θ (black) and the activity bump phase (yellow) are overlaid. (**b**) The connectivity matrix from the model visual neuron to the model HD neurons, after the experiment in (a), which was initially uniformly 0. As described in Fig. 3a, a unique mapping from a visual landmark to the bump position was learned. (**c**) The offset between θ and the bump phase (pink), as well as the distribution of peak positions of the scene-bump offset (grey) over 100 repetitions of the simulation (i.e., μ from von Mises fits on the scene-bump offset histograms). The peak position appeared uniformly distributed over repetition – that is, the scene was anchored to the HD neurons with an arbitrary offset, as seen in the real fish (Fig. 1g and Extended Data Fig. 2f). (**d**) The model HD neuron outputs from a simulated experiment, where the visual scene switched from the Sun-and-bars scene to the Stonehenge scene halfway through (as in Extended Data Fig. 4a–g). (**e**) The scene-bump offset histogram for the simulated data in (d), separately for the two visual scenes, as in Extended Data Fig. 4c (**f**) The distribution of the κ parameter from the von Mises fit on the scene-bump offset histograms over 100 repetitions of the simulation. As a reference, the highest scene-bump offset κ we observed in the experimental data was around 4, suggesting that the model tracked the two scenes as well as or better than fish most of the time. (**g**) The distribution of the difference in the μ parameter from von Mises fits on the scene-bump offset histograms between the two scenes (i.e., differences of the peak positions). The radial axis represents the density. Peak difference was biased around $\pi/2$ similar to the experimental data (Extended Data Fig. 4e; see also Supplementary Note 1 for how the model visual cells responded to each scene). (**h**) The model HD neuron outputs from a simulated experiment, where the Sun-and-bars scene smoothly rotated about the observer ("Smooth" epoch) or abruptly jumped ("Jump" epoch), or a feature-less binary noise rigidly rotated about the observer ("Noise" epoch) (as in Fig. 2). (**i**) The scene-bump offset histogram from the data in (h), separately for each epoch, as in Fig. 2e. (**j**) The distribution of the von Mises κ parameters from fits on the scene-bump offset histograms, over 100 simulation repetitions. The model performs much better than real fish in the Noise epoch, because the model is specifically calibrated to perform unity-gain angular path integration (Supplementary Note 1). More notably, a short (4 min) experience in the "Smooth" epoch was enough to establish strong enough visual-to-HD connectivity capable of instructing the bump phase. (**k**) The outputs of the model HD neurons in an experiment where the observer experiences scenes with a single sun-like spots (pre- and post-learning epochs) or two suns (learning epoch) as in Fig. 3b. In this particular run, the bump phase tracked the scene very well in the double-sun epoch, but the experience in the double sun epoch introduced more errors in the Post epoch. (**l**) The visual-to-HD connectivity after each epoch from the particular simulation run shown in (k). Even though the bump faithfully tracked one of the sun presented during the learning epoch, each model HD neuron was always co-activated with an antipodic pair of visual neurons, resulting in the doubled connectivity (as illustrated in Fig. 3a). (**m**) The distribution of the scene-bump offset histograms, separately for each epoch, as in Fig. 3d. (**n**) The distribution of the fraction of the time where the absolute scene-bump offset was above $3\pi/4$, over 100 simulation repetitions, similar to Fig. 4e. The fraction was initially always below 0.1 in the pre-learning epoch, then went up in the learning epoch, and did not sometimes come back in the post-learning epoch, just like in the real data.

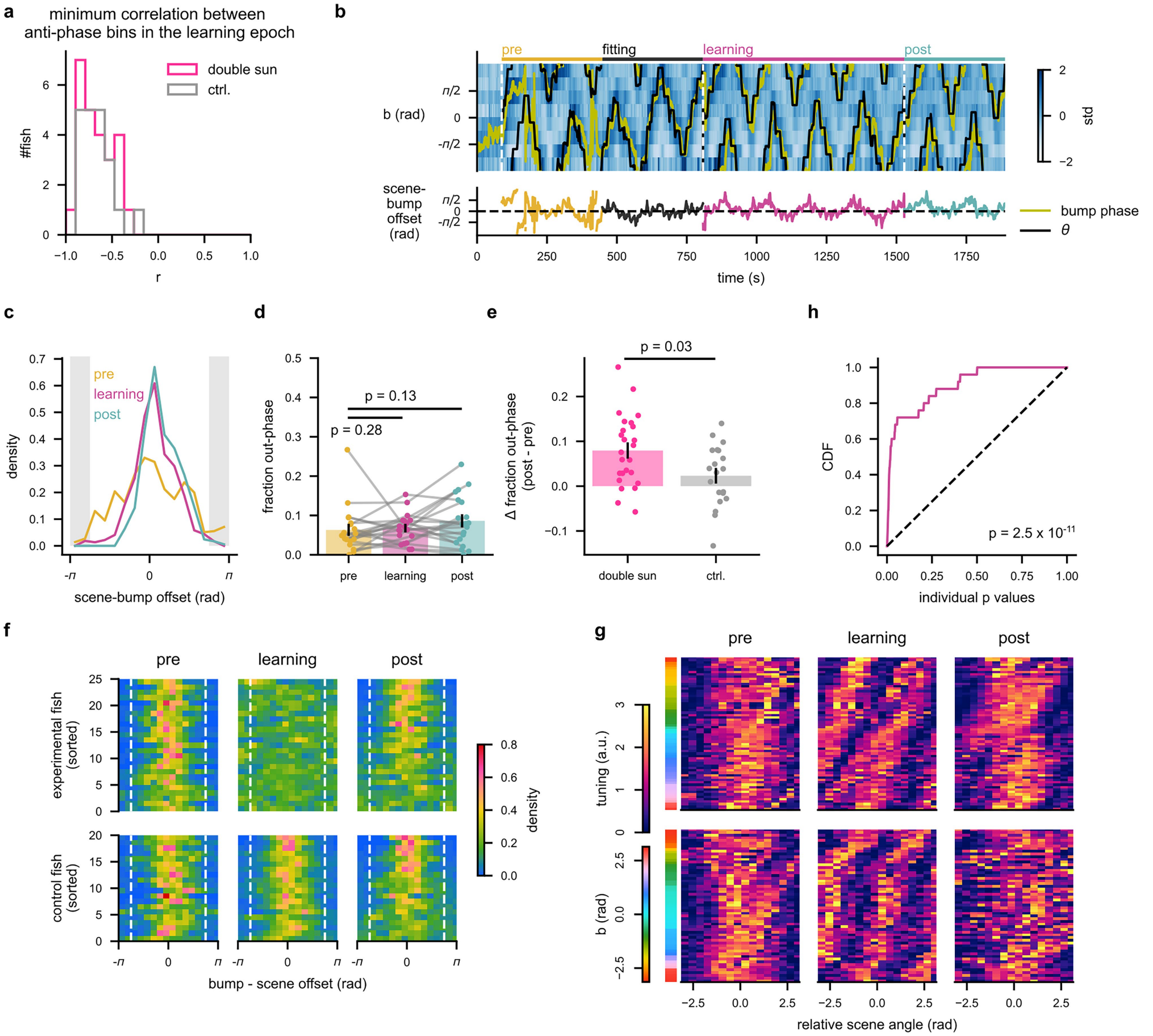

Extended Data Fig. 7 | Further characterizations of the remapping experiment. (**a**) The distributions of the minimum Pearson correlations between pairs of HD neuron bins with the opposite scene orientation tunings, during the learning epochs. Antipodic pairs of HD cells remained anti-correlated, even in the symmetric scene. (**b**) Data from an example fish in the control experiment, as in Fig. 3c. (**c**) The distribution of the scene-bump offset for each epoch, for the same fish as shown in (c). (**d**) The fractional time that the bump-scene offset spent in the out-phase range, for each epoch in the control experiment. No significant increase was detected (sign-rank test). N = 20 fish. (**e**) Increase in the fraction of time that the offset spent in the out-phase range from the pre- to post-learning epoch was significantly higher in the double-sun experiment, compared to the control experiment (rank sum test, N = 25 fish for the double-sun experiment, 20 fish for the controls). (**f**) The histograms of the scene-bump offset from all fish in either condition, separately for each epoch. (**g**) The centered tuning of the HD neurons in each epoch sorted by the preferred orientation b, as in Fig. 4a, but from two more example fish. (**h**) The cumulative distribution of the p-values from bootstrap tests on the von Mises κ fit on the 2θ - bump offset in the symmetric scene, as in Fig. 4i. The distribution of the p-values was significantly non-uniform based on a Kolmogorov-Smirnov test ($p = 2.5 \times 10^{-11}$; N = 25 fish). For (d, e), the bars and error bars respectively indicate means across fish and their standard errors.

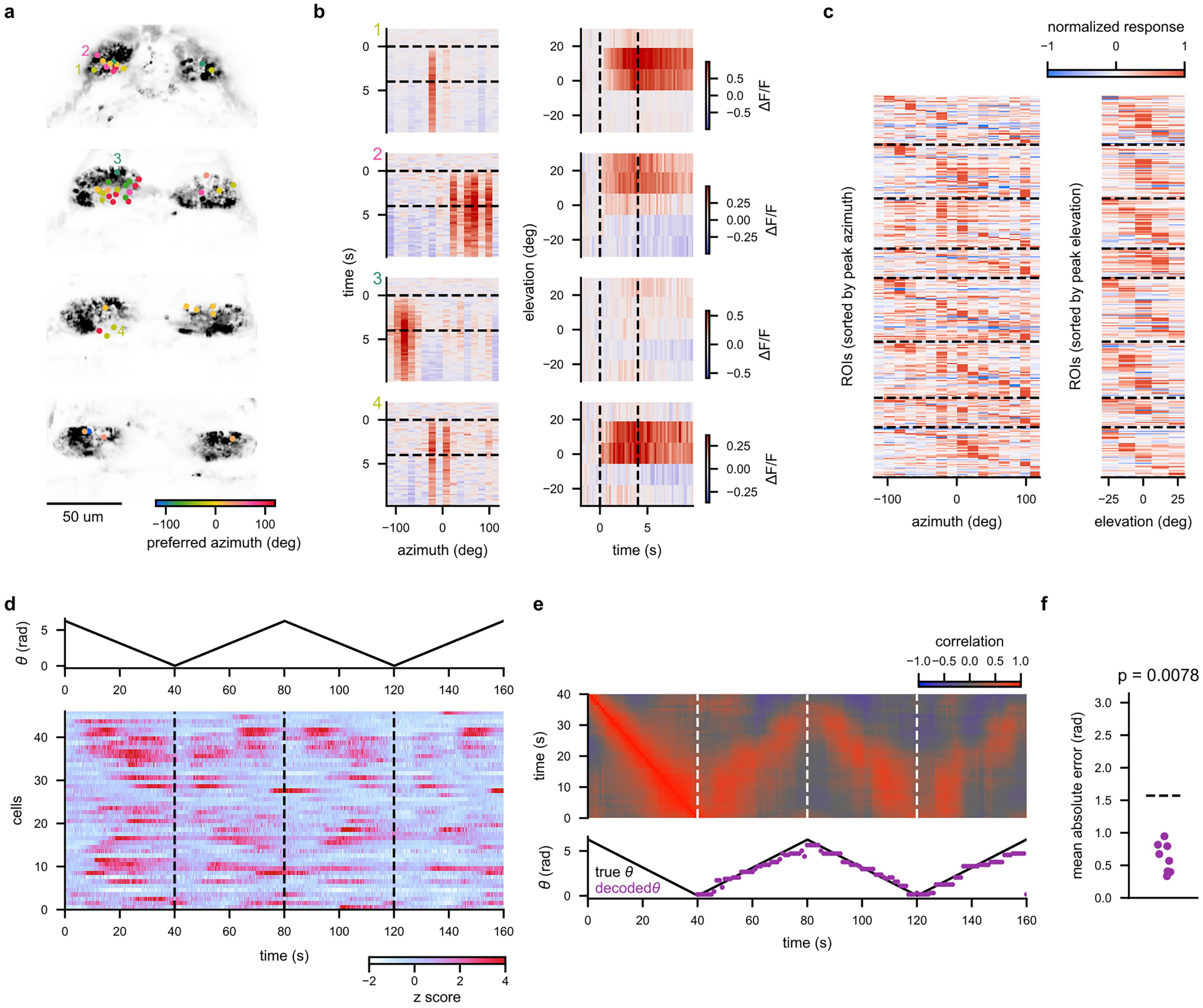

Extended Data Fig. 8 | The habenula encodes sufficient visual information to disambiguate the scene orientation. (**a**) The anatomy of habenula neurons labeled by vglut2a:Gal4, plane by plane from dorsal to ventral, 10 microns apart. The dots indicate the location of the visually responsive ROIs, color-coded by their preferred azimuth. Visually responsive cells were enriched in the dorsal left nucleus as reported before[21], and no retinotopy was apparent[23]. (**b**) The responses of selected neurons to (*left*) vertical bright bars at different azimuths, and (*right*) horizontal bright bars at different elevations, over time. The locations of the cell bodies of these cells are indicated by numbers in (a). (**c**) The time-averaged bar responses over azimuth and elevation for each ROI, concatenated over multiple fish (dotted horizontal lines separate individual animals). The ROIs are sorted within each fish, separately for vertical and horizontal bar responses by their peak locations. The peaks of the bar responses were broadly distributed in each fish, indicating that local receptive fields of the habenula neurons tile the visual space. (**d**) (*bottom*) The normalized responses of the visually responsive habenula neurons to the Sun-and-bars scene, slowly rotating about the fish four times in alternating senses (*top*). (**e**) (*top*) The correlation of the instantaneous activity patterns of habenula neurons between a time point within the first 40 s (on the y-axis) and another time point anywhere during the experiment (on the x-axis). To calculate these correlations, the neural data was downsampled to 1 Hz. The zig-zag diagonal pattern of high correlation mirroring the scene orientation θ is apparent, suggesting that the habenula neurons showed similar activities when the scene was at similar orientations. (*bottom*) For each time point, we decoded θ by looking for the time point with in the first 40 s where the habenula activity correlated the best with the ongoing pattern of habenula activity and taking θ at that time point (purple dots). (**f**) The time-averaged absolute error between the true and decoded θ. Each dot represents a single fish. The absolute error was significantly below the chance level ($\pi/2$, dotted line), from a signed-rank test. N = 8 fish.

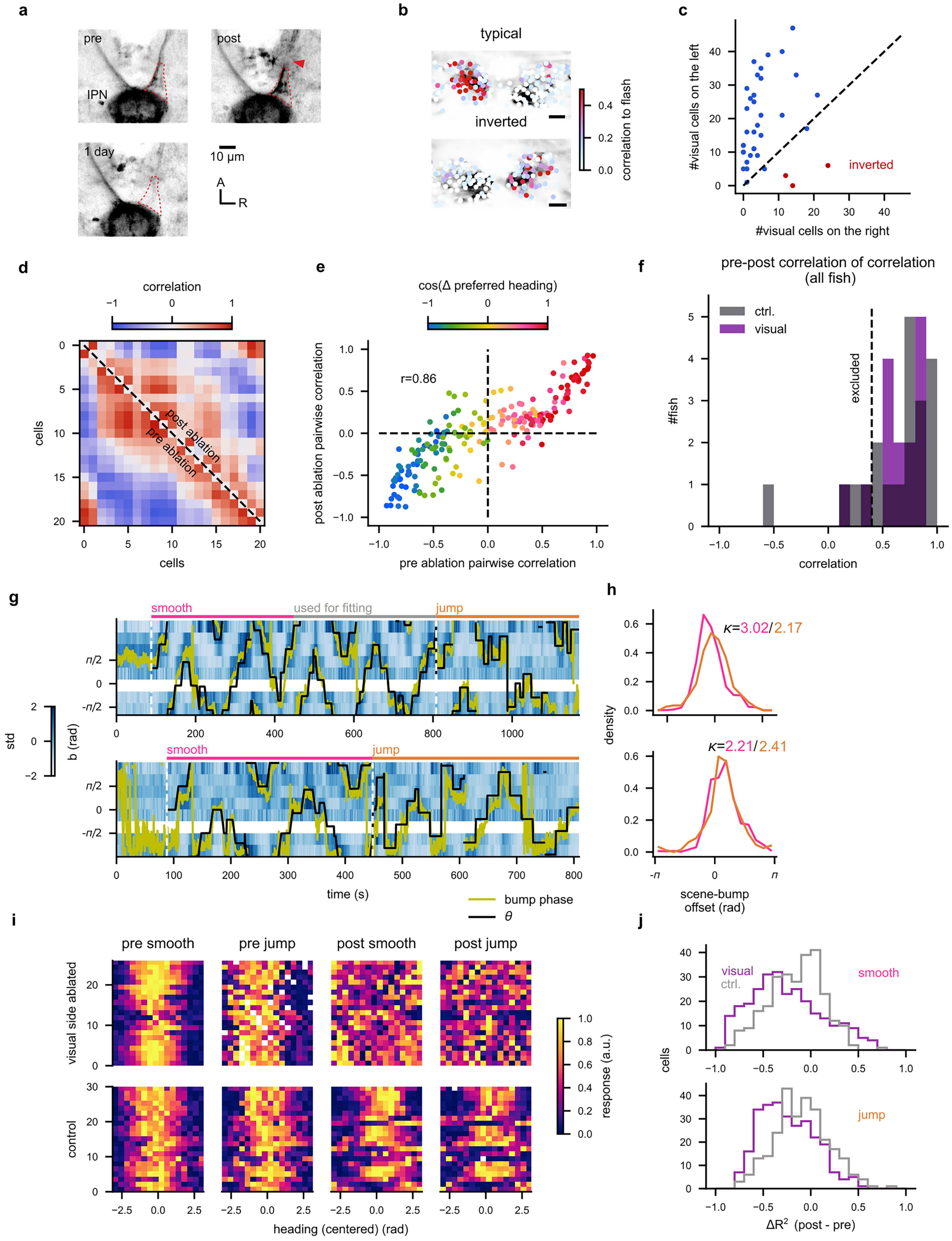

Extended Data Fig. 9 | See next page for caption.

Extended Data Fig. 9 | Additional details of the ablation experiment. (**a**) The axons of the habenula neurons entering the IPN, before, right after, and 1 day after the ablation procedure. The ablated site is marked by the red arrow. The neuronal processes between the ablation site and the IPN initially increased the fluorescence, and the disappeared (red dotted line). The same procedure was repeated on all 37 fish tested. (**b**) Two examples of fish with the typical and inverted habenula laterality. The ROIs are color-coded by the average pairwise correlations of their responses to the repeated presentations of the flash stimuli. The scale bars indicate 10 µm. (**c**) The numbers of the habenula ROIs that had averaged flash correlation beyond 0.3 on each side, plotted against each other. The red dots represent fish with the inverted habenula laterality. N = 37 fish, including ones that were excluded from the final analyses of the ablation effects (see Methods for the criteria). (**d**) The correlation matrices of the HD neuron activity in the pre-ablation (lower triangle) and post-ablation recordings (upper triangle), in the same example fish as in Fig. 5c. The cells are sorted by their preferred scene orientation. (**e**) The pairwise correlation between all pairs of HD neurons from the pre- and post-ablation recordings in the same fish, plotted against each other. The cell pairs are colored by the cosine of the difference of their scene orientation tunings. The correlation structure among the HD cells were well maintained in this fish after the ablation. (**f**) The distributions of the correlations of pairwise HD cell correlations before and after the ablations. Fish with correlation lower than 0.4 were excluded from the analysis. (**g, h**) The binned HD cell activities (**g**) and the scene-bump offset histograms (**h**) as in Fig. 5c,d, but for an example fish with the control side ablation. (**i**) The centered tuning of the HD cells from a pair of example fish in visual side ablated and control groups (the same as in Fig. 5c,g), for each epoch of each recording. The visual side ablation appears to more or less uniformly abolish the scene orientation tuning in this particular example. (**j**) To quantify the change in tuning caused by habenula ablation at the single neuron level, we fit scaled, shifted sinusoids to individual HD cell tuning, separately for each epoch in each recording, and calculated the difference in the goodness-of-fit metric (R^2) across recordings, which is plotted here as a histogram (concatenated across animals). A: anterior; R: right.

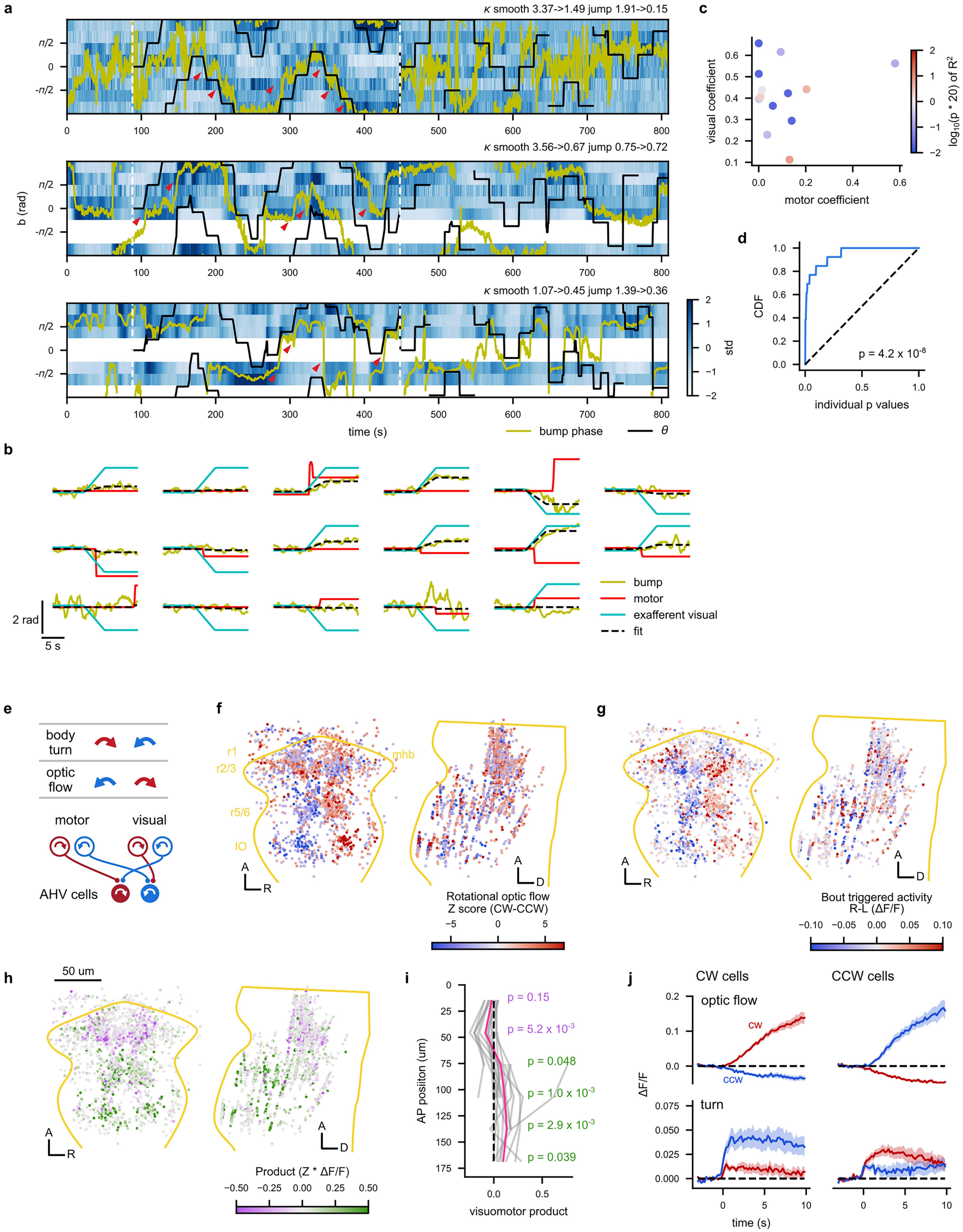

Extended Data Fig. 10 | See next page for caption.

Extended Data Fig. 10 | Putative mechanisms of angular path integration. (**a**) The post-ablation binned HD cell activities from several example fish (with visual-side ablations) as in Fig. 5c. Places where the bump phase appeared to move as the scene rotated are indicated by the red arrows. (**b**) To test if these bump movements are statistically meaningful, we regressed the bump phase (yellow) around the scene rotation episodes with the cumulative turns ("motor", red) and the exafferent scene rotations (cyan), as in Extended Data Fig. 5d, for the smooth epoch in the post-ablation recordings of the visual side-ablated group. The fitted curves are in dotted black. The data from the same fish in Fig. 5c are shown. (**c**) The visual and motor coefficients from the regression analysis, averaged over rotation episodes, plotted against each other. The colors indicate the p-values from the bootstrap tests on the episode-averaged R^2 value. The colors are scaled with $\log_{10}(20^*p)$, so that $p < 0.05$ appear blue. 10 fish out of 13 showed significantly above chance fit. (**d**) The distribution of the bootstrap-based, fish-wise p-values in (c) was significantly non-uniform, based on Kolmogorov-Smirnov test ($p = 4.2 \times 10^{-8}$, N = 13 fish). (**e**) As an observer turns one way, it perceives rotational optic flow in the opposite sense. As such, if there exist a multi-modal angular head velocity (AHV) cells, they should be activated by motor commands and rotational optic flows in the opposite senses. (**f**) Hindbrain ROIs that reliably responded to rotational optic flow are shown in the (*left*) horizontal or (*right*) sagittal projection. The ROIs are color-coded by the Z-scored differences in their response to clockwise (CW) and counterclockwise (CCW) stimuli. Note how rotation direction-selective cells are widely distributed at different rhombomeres, but they generally prefer ipsiversive rotations, with the exception of r2/3. See also Supplementary Video 3. (**g**) Same as (f), but ROIs are now color-coded by the difference in turn-triggered activities by directions (in the unit of $\Delta F/F$). Similar to the visual direction selectivity, the ROIs generally preferred ipsiversive turns. The r1 contained bilateral clusters of cells with contraversive motor preference. (**h**) Same as (f, g), but the ROIs are colored by the product of the visual and motor related activity differences. Rhombomeres 1 through 2/3 have clusters of cells with negative visuo-motor products, as expected of AHV cells. Cells in the posterior rhombomeres, in contrast, generally had positive visuo-motor produces, a phenomenology consistent of cancellation of expected reafference. (**i**) Binned averaged visuo-motor products along the anterior-posterior axis. Grey lines are from individual fish, and the pink line is the average. Each bin was tested against 0 with signed-rank tests (N = 13, 16, 20, 18, 11, 8 fish from anterior to posterior). (**j**) The average visual and motor responses of the cells in the second bin (approximately corresponding to r2/3), separately for their directional tuning. The solid lines and shades around them respectively indicate mean across fish and its standard error. N = 16 fish. r1: rhombomere 1; r2/3: rhombomere 2/3; r5/6: rhombomere 5/6; IO: inferior olive; mhb: midbrain-hindbrain boundary; A: anterior; R: right; D: dorsal.

nature portfolio

Corresponding author(s): Ruben Portugues

Last updated by author(s): 2025.11.07

Reporting Summary

Nature Portfolio wishes to improve the reproducibility of the work that we publish. This form provides structure for consistency and transparency in reporting. For further information on Nature Portfolio policies, see our Editorial Policies and the Editorial Policy Checklist.

Statistics

For all statistical analyses, confirm that the following items are present in the figure legend, table legend, main text, or Methods section.

n/a	Confirmed	
☐	☒	The exact sample size (n) for each experimental group/condition, given as a discrete number and unit of measurement
☐	☒	A statement on whether measurements were taken from distinct samples or whether the same sample was measured repeatedly
☐	☒	The statistical test(s) used AND whether they are one- or two-sided *Only common tests should be described solely by name; describe more complex techniques in the Methods section.*
☐	☒	A description of all covariates tested
☐	☒	A description of any assumptions or corrections, such as tests of normality and adjustment for multiple comparisons
☐	☒	A full description of the statistical parameters including central tendency (e.g. means) or other basic estimates (e.g. regression coefficient) AND variation (e.g. standard deviation) or associated estimates of uncertainty (e.g. confidence intervals)
☐	☒	For null hypothesis testing, the test statistic (e.g. F, t, r) with confidence intervals, effect sizes, degrees of freedom and P value noted *Give P values as exact values whenever suitable.*
☒	☐	For Bayesian analysis, information on the choice of priors and Markov chain Monte Carlo settings
☒	☐	For hierarchical and complex designs, identification of the appropriate level for tests and full reporting of outcomes
☐	☒	Estimates of effect sizes (e.g. Cohen's d, Pearson's r), indicating how they were calculated

Our web collection on statistics for biologists contains articles on many of the points above.

Software and code

Policy information about availability of computer code

Data collection	Two-photon imaging data were acquired using a python-based, custom-written software, which interfaced with an FPGA controlling a resonant-galvo scanning head through the National Instruments modular instruments python API (nimi-python). The FPGA was running a custom LabView code (LabView 2015) to control the scanning and the data acquisition (Varga et al. 2011 PNAS). Stimulus presentation and tail-tracking were performed using the Stytra 0.8 package (https://github.com/portugueslab/stytra).
Data analysis	All two-photon imaging data were pre-processed with the suite2p 0.10 package. The code for the subsequent analyses are available from our github repository (https://github.com/portugueslab/Tanaka_2025_landmark). The scripts were written in python 3.10, within the framework of Jupyterlab 3.4. General numerical operations were performed using numpy 1.22, and more complex operations (convolution, binning, statistics, curve fitting) used scipy 1.9 as well as scikit-learn 1.1.2. The data were visualized using matplotlib 3.6.

For manuscripts utilizing custom algorithms or software that are central to the research but not yet described in published literature, software must be made available to editors and reviewers. We strongly encourage code deposition in a community repository (e.g. GitHub). See the Nature Portfolio guidelines for submitting code & software for further information.

Data

Policy information about availability of data

All manuscripts must include a data availability statement. This statement should provide the following information, where applicable:

- Accession codes, unique identifiers, or web links for publicly available datasets
- A description of any restrictions on data availability
- For clinical datasets or third party data, please ensure that the statement adheres to our policy

All the source data from the functional experiments (ROI-wise fluorescent traces, anatomical ROI maps, behavioral traces, and traces of the stimulus states), as well as anatomical stacks used to generate the images in the figures are deposited on a Zenodo repository (DOI: 10.5281/zenodo.17233579). The anatomical stack for the 18107:Gal4 driver line is available from Z Brain Atlas (https://zebrafishexplorer.zib.de).

Research involving human participants, their data, or biological material

Policy information about studies with human participants or human data. See also policy information about sex, gender (identity/presentation), and sexual orientation and race, ethnicity and racism.

Reporting on sex and gender	N/A
Reporting on race, ethnicity, or other socially relevant groupings	N/A
Population characteristics	N/A
Recruitment	N/A
Ethics oversight	N/A

Note that full information on the approval of the study protocol must also be provided in the manuscript.

Field-specific reporting

Please select the one below that is the best fit for your research. If you are not sure, read the appropriate sections before making your selection.

☒ Life sciences ☐ Behavioural & social sciences ☐ Ecological, evolutionary & environmental sciences

For a reference copy of the document with all sections, see nature.com/documents/nr-reporting-summary-flat.pdf

Life sciences study design

All studies must disclose on these points even when the disclosure is negative.

Sample size	Due to the novel nature of hte phenomenology we studied, it was difficult to estimate the effect size and individual variability beforehand. As such, we did not pre-calculate the sample size (the number of fish). Instead, we initially aimed to collect data from about 20 animals per experiment or per condition (where an experiment involved comparisons across different groups of animals), following other studies using the larval zebrafish. Since the first experiment (Fig. 1) with about 20 fish allowed us to observe relevant physiology of the head-direction (HD) neurons consistently (as statistically qunatified with a Kolmogorov-Smirnov test in Extended Data Fig. 2e), we decided to pursue similar samples sizes in the following experiments on the HD neurons as well (Fig. 2-5, Extended Data Fig. 3, 4a-g). We have smaller sample sizes in some cases: For extended Data Fig. 4h-m (N = 12 fish), we collected less data due to the supplementary nature of the experiment. For Fig. 5, we ended up with 12 to 15 fish per condition, due to the exclusion that were necessary for a tighter quality control for across-fish / across-recording comparisons. For the recording of visual resposnes in habenula (N = 8 fish), we collected less data because we expected less individual variability due to the peripheral, sensory nature of the neurons of interest.
Data exclusions	As stated in the Materials and Methods section, in all experiments, recordings where we could not identify a group of head-direction (HD) neurons covering at least 5 out 8 45 degree bins of the head direction angles were excluded from further analyses. This is because it was difficult to estimate the internal heading estimate by the HD cells in such recordings. In addition, in Extended Data Fig. 3, fish with less than 5 reliable swim bouts were excluded, as it made correlating neural data with behavior unreliable. In Fig. 3 and 4, recordings where the HD cell activity bump amplitude decayed more than 60% between the pre- and post-learning epochs were excluded, as it made assessing the change in bump-scene alignment unreliable. In Fig. 5, fish where the correlation structure among the HD cells changed between the pre- and post-ablation recordings (correlation of corrleation < +0.4) were excluded. The change in correlation structure likely represent our failure to identify the same imaging plane across the ablation and/or poor health of the animal. In addition, fish whose HD cell bump did not align well enough in the pre-ablation recordings (tkappa < +0.5 from von Mises fit on the bump-scene offset distribution) were excluded, because it was difficult to assess the effect of ablation in such fish.
Replication	All our findings are based on observations from experiments repeated on around 20 animals, as stated above.

Randomization	Animals were selected randomly from clutches of larvae for experiments, and assigned to different groups randomly, where there were multiple groups of animals (Fig. 3-5).
Blinding	In Fig. 3 and 4, the experimenter were not blinded to the groups of animals, as they needed to initiate different stimulus protocols according to the group each animal was assigned to. In Fig. 5, the experimenter did not know whether the ablated side was visually reponsive or not unitl the data analysis, although this sidedness was heavily biased (Extended Data Fig. 9c).

Reporting for specific materials, systems and methods

We require information from authors about some types of materials, experimental systems and methods used in many studies. Here, indicate whether each material, system or method listed is relevant to your study. If you are not sure if a list item applies to your research, read the appropriate section before selecting a response.

Materials & experimental systems

n/a	Involved in the study	
☒	☐	Antibodies
☒	☐	Eukaryotic cell lines
☒	☐	Palaeontology and archaeology
☐	☒	Animals and other organisms
☒	☐	Clinical data
☒	☐	Dual use research of concern
☒	☐	Plants

Methods

n/a	Involved in the study	
☒	☐	ChIP-seq
☒	☐	Flow cytometry
☒	☐	MRI-based neuroimaging

Animals and other research organisms

Policy information about studies involving animals; ARRIVE guidelines recommended for reporting animal research, and Sex and Gender in Research

Laboratory animals	Zebrafish (Danio rerio) from Tuepfel long ifn (TL) strain, 6-9 days post fertilization.
Wild animals	No wild animals were used in the study.
Reporting on sex	All animlas were of yet undetermined sex.
Field-collected samples	No field-collected samples were used in the study.
Ethics oversight	The animal handling and experiments were performed according to protocols approved by the animal welfare officer at Institut für Neurowissenschaften, Technische Universität München (TUM) and the relevant department of the regional government (Regierung von Oberbayern, Sachgebiet 55.2) (animal protocol number 55-2-1-54-2532-1011 and 55.2-2532.Vet_022-24-5).

Note that full information on the approval of the study protocol must also be provided in the manuscript.

Plants

Seed stocks	N/A
Novel plant genotypes	N/A
Authentication	N/A